

Statistical analysis of $m/n = 2/1$ locked and quasi-stationary modes with rotating precursors at DIII-D

R. Sweeney¹, W. Choi¹, R.J. La Haye², S. Mao^{3,+}, K.E.J. Olofsson^{1,*}, F.A. Volpe¹, and the DIII-D Team

¹ Columbia University, New York, NY 10027

² General Atomics, San Diego, CA 92121

³ University of Wisconsin, Madison, WI 53706

+ Present address: Stanford University, Stanford, CA 94305

* Present address: General Atomics, San Diego, CA 92121

Abstract.

A database has been developed to study the evolution, the nonlinear effects on equilibria, and the disruptivity of locked and quasi-stationary modes with poloidal and toroidal mode numbers $m = 2$ and $n = 1$ at DIII-D. The analysis of 22,500 discharges shows that more than 18% of disruptions are due to locked or quasi-stationary modes with rotating precursors (not including born locked modes). A parameter formulated by the plasma internal inductance l_i divided by the safety factor at 95% of the toroidal flux, q_{95} , is found to exhibit predictive capability over whether a locked mode will cause a disruption or not, and does so up to hundreds of milliseconds before the disruption. Within 20 ms of the disruption, the shortest distance between the island separatrix and the unperturbed last closed flux surface, referred to as d_{edge} , performs comparably to l_i/q_{95} in its ability to discriminate disruptive locked modes. Out of all parameters considered, d_{edge} also correlates best with the duration of the locked mode. Disruptivity following a $m/n = 2/1$ locked mode as a function of the normalized beta, β_N , is observed to peak at an intermediate value, and decrease for high values. The decrease is attributed to the correlation between β_N and q_{95} in the DIII-D operational space. Within 50 ms of a locked mode disruption, average behavior includes exponential growth of the $n = 1$ perturbed field, which might be due to the $2/1$ locked mode. Surprisingly, even assuming the aforementioned $2/1$ growth, disruptivity following a locked mode shows little dependence on island width up to 20 ms before the disruption. Greater deceleration of the rotating precursor is observed when the wall torque is large. At locking, modes are often observed to align at a particular phase, which is likely related to a residual error field. Timescales associated with the mode evolution are also studied and dictate the response times necessary for disruption avoidance and mitigation. Observations of the evolution of β_N during a locked mode, the effects of poloidal beta on the saturated width, and the reduction in Shafranov shift during locking are also presented.

1. Introduction

Rotating and non-rotating ("locked") neoclassical tearing modes (NTMs) are known to degrade confinement and cause disruptions in tokamak plasmas under certain plasma conditions, and thus represent a concern for ITER [1].

NTMs can rotate at the local plasma rotation velocity, apart from a small offset of the order of the electron or ion diamagnetic velocity [2]. In present tokamaks with strong torque injection, this corresponds to rotation frequencies of several kHz. Magnetic islands can also steadily rotate at frequencies of the order of the inverse resistive-wall time (tens of Hz, typically), if a stable torque balance can be established at that frequency. In that case, they are called Quasi Stationary Modes (QSMs) [3].

There are also NTMs that do not rotate at all, called Locked Modes (LMs). Some of these are the result of an initially rotating NTM ("rotating precursor") decelerating and locking to the residual error field. The deceleration might be due, for example, to the magnetic braking experienced by the rotating island in its interaction with the eddy currents that it induces in the resistive wall [4]. Other modes are "born locked", i.e. they form without a rotating precursor, as a result of resonant error field penetration.

It will be important to understand the onset, growth, saturation and stabilization of all these categories of rotating and non-rotating NTMs, in order to maintain good confinement and prevent disruptions in ITER. Here we present an extensive analysis of QSMs and LMs with rotating precursors, which we will sometimes refer to as "initially rotating locked modes", or IRLMs. The analysis was carried over approximately 22,500 DIII-D [5] plasma discharges, and restricted to poloidal/toroidal mode numbers $m/n=2/1$ because these are the mode numbers that are most detrimental to plasma confinement in DIII-D and most other tokamaks [6]. QSMs and LMs of different m/n (for example $3/2$, occasionally observed at DIII-D) and LMs not preceded by rotating precursors are not considered here and will be the subject of a separate work.

Works have described classical [7, 8] and neoclassical [9, 6, 10] tearing modes (TMs), and torques on TMs [4]. Effects of TMs on confinement are described theoretically [11]. Summaries are written for error-field-penetration locked modes on DIII-D [12], for disruption phenomenology in JET [13], and for disruption observations across many machines [14].

Disruption statistics of plasma equilibrium parameters and MHD stability limits are investigated at JET [15] and provide detailed accounting of the instabilities preceding disruptions [16]. A comprehensive study of disruptivity as a function of various equilibrium pa-

rameters was conducted at NSTX [17] followed by a work on disruption prediction including $n = 1$ locked mode parameters [18]. A brief study of disruptivity as a function of the safety factor and the normalized plasma beta on DIII-D has been reported [19].

Machine learning approaches to disruption prediction have shown rather high levels of success at ASDEX Upgrade [20, 21], JET [22], and JT-60U [23], and a predictor tuned on JET was ported to ASDEX Upgrade [24]. Similarly, neural networks have been used for disruption prediction at TEXT [25], and ADITYA [26], and for predicting ideal stability boundaries on DIII-D [27]. Discriminant analysis for disruption prediction was conducted at ASDEX Upgrade [28].

A statistical work on MAST investigated the differences between disruptive and non-disruptive LMs as a function of normalized plasma beta and the safety factor [29]. Recently a locked mode thermal quench threshold has been proposed based on equilibrium parameters from studies on JET, ASDEX Upgrade, and COMPASS [30]. The automatic detection of locked modes with rotating precursors makes the disruption statistics presented here unique. In addition, this work includes basic observations of locked modes and their effects on equilibria.

During the first discharges in this database, DIII-D was equipped with one poloidal and four toroidal arrays of Mirnov probes and saddle loops [32]. During the time spanned by the database, additional sensors were added for increased 3D resolution [33]. However, a limited set of six saddle loop sensors (external to the vessel) and three poloidal sensors (inside the vessel) are used for simplicity, and for consistency of the analysis across all shots, spanning the years 2005-2014.

An example of the $2/1$ IRLMs considered here is illustrated in Fig.1. The poloidal field amplitude of the rotating precursor is detected by the toroidal array of Mirnov probes around 1800 ms. The mode simultaneously grows and slows down until it locks at 1978.5 ms. Due to the finite binning time for Fourier analysis during the rotating phase, the rotating signal is lost at low frequency, and is instead measured by a set of large saddle loops (ESLDs: external saddle loops differenced). The response of the saddle loops increases when $\omega < \tau_w^{-1}$, where $\tau_w \sim 3$ ms is the characteristic $n = 1$ wall time for DIII-D. As shown in Fig.1, it is not uncommon for the amplitude of an IRLM to oscillate due to minor disruptions, and to grow prior to disruption (see section 6.2).

Three interesting results of this work are introduced now. First, it will be shown that the $m/n = 2/1$ island width cannot be used to predict disruptions 20 ms or more ahead of time. Similarly, the island width shows little correlation with the IRLM survival time.

Second, the plasma internal inductance divided

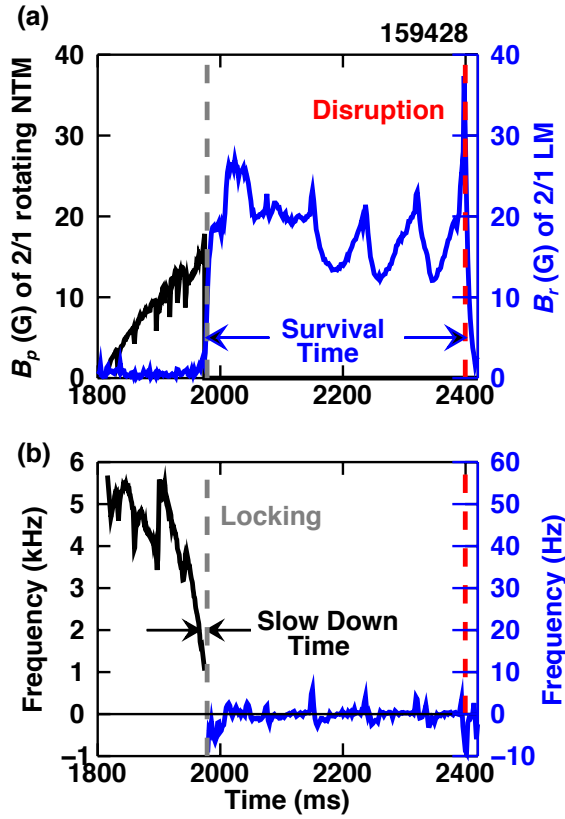


Figure 1. Example of an initially rotating locked mode (IRLM). The black trace presents a fast rotating 2/1 NTM, as measured by the set of Mirnov probes and analyzed by *eigspec*[31]. At the time of locking (1978.5 ms), the low frequency mode is detected by the ESLDs, shown in blue. The slow-down time is the time taken for a mode rotating at 2 kHz to slow and lock; survival time is the duration of an IRLM that ends in a disruption. A factor of 0.5 has been multiplied to the Mirnov probes signal to account for the eddy currents in the wall during fast mode rotation. A factor of 2 has been multiplied to the ESLD signal to obtain the peak radial magnetic field from the measurement averaged over the large ESLD area.

by the safety factor, l_i/q_{95} , distinguishes LMs that will disrupt from those that will not. The predictive capability of l_i/q_{95} might be related to the energy available to drive nonlinear island growth.

Finally, a spatial parameter which couples the $q = 2$ radius and the island width, referred to as d_{edge} (see section 5 for definition), distinguishes disruptive from non-disruptive LMs comparably to l_i/q_{95} within 20 ms of the disruption. It also correlates best with the locked mode survival time. The predictive capability of d_{edge} is believed to be related to the physics of the thermal quench.

The paper is organized as follows. Section 2 explains the method of detection of disruptions, of rotating tearing modes, and of LMs. Section 3 provides some general statistics of IRLM occurrences in DIII-D.

Section 4 quantifies the timescales of interest before locking. Section 5 investigates the time available to intervene before an IRLM causes a disruption. Section 6 discusses the width and phase behavior at locking, and the exponential growth of the $n = 1$ field before the disruption. Section 7 details the interdependence between IRLMs and plasma β ($\beta = \langle p \rangle / (B^2 / 2\mu_0)$ where $\langle p \rangle$ is the average pressure and B is the average total field strength). Section 8 decouples the influence of ρ_{q2} , q_{95} , and l_i on IRLM disruptivity, and investigates the effectiveness of l_i/q_{95} , the island width, and d_{edge} as disruption predictors. A discussion section follows which offers possible explanations of the physical relevance of l_i/q_{95} and d_{edge} . Finally, two appendices are dedicated to the mapping from radial magnetic field measurements to the perturbed island current, and from the perturbed current to an island width.

2. Method

2.1. Detection of disruptions

To categorize disruptive and non-disruptive modes, a clear definition of disruption is needed. The plasma current decay-time is used to differentiate disruptive and non-disruptive plasma discharges. The decay-time t_D is defined as the time taken by the plasma current I_p to decay from 80% to 20% of its flat-top value, divided by 0.6, as was done for disruption studies on JET [34].

The criterion to identify DIII-D disruptions, $t_D < 40$ ms, was formulated as follows.

A histogram of all decay-times is shown in figure 2, where three populations are observed. The first group peaks near $t_D = 0$ and extends up to $t_D = 40$ ms. These are rapid losses of I_p and confinement, quicker than typical energy and particle confinement times. Discharges in this group are categorized as major disruptions, occurring during the I_p flat-top. It is worth noting that of the 5,783 disruptions detected, 666 occurred within the first second (in the ramp-up phase), none of which were caused by an IRLM. At the opposite limit, group *iii*, with $t_D > 200$ ms, contains only non-disruptive discharges, in which the plasma current decays as programmed. Population *ii* has t_D in the range $40 \text{ ms} < t_D < 200 \text{ ms}$, and mostly consists of shots that disrupted during the current ramp-down.

Note that while the stringent threshold of $t_D < 40$ ms will prevent falsely categorizing non-disruptive discharges as disruptive, it may also categorize a few disruptions with slightly longer decay times into group *ii*. However, the thresholds are chosen to protect against false positives better than false negatives; they are chosen to compromise missing a number of disruptive shots in exchange for ensuring the validity of all disruptive discharges. In a manual verification

of 50 discharges which were identified as disruptive according to the $t_D < 40$ ms criterion, no false positives were found. Unless otherwise noted, the title of "disruption" will be reserved for major disruptions that occurred during the I_p flat-top, for reasons discussed below.

In section 3, disruptivity will be studied over the entire database, including shots that did not contain IRLMs. We will refer to disruptivity in this context as *global disruptivity* (i.e. the number of disrupted discharges divided by all discharges).

In all sections following section 3, disruptivity will be studied on shots that contained IRLMs only, and will be referred to as *IRLM disruptivity* (i.e. the number of shots that disrupt with an IRLM divided by all shots with IRLMs). Studying IRLM disruptivity will allow us to investigate what makes a disruptive IRLM unique, and thus provide insight into the physics of these disruptions.

2.2. IRLM Disruptivity during current flat-tops

For all IRLM disruptivity studies, disruptions that occur during I_p ramp-downs are omitted. I_p ramp-downs are characterized by major changes of the plasma equilibrium, and are expected to greatly impact the locked mode evolution. Namely, key parameters such as q_{95} , l_i , and ρ_{q2} evolve during an I_p ramp-down, complicating the interpretation of their effect on IRLM disruptivity. Similarly, I_p ramp-downs are found to be effective at avoiding disruptions (as will be shown in section 8.6), and therefore an IRLM that terminates benignly during an I_p ramp-down might have disrupted otherwise. Moreover, flat-tops will be longer and longer in ITER and DEMO, thus disruptivity during ramp-down will become less and less important. Eventually, in a steady-state powerplant, only flat-top disruptivity should matter. Hence, discharges which contain a locked mode during the I_p ramp-down, regardless of whether the plasma disrupts during ramp-down or not, are excluded from IRLM disruptivity studies here.

Out of 1,113 shots which disrupted due to an IRLM, 105 contained an additional IRLM distinct in time from the final disruptive one. As these additional IRLMs decayed or spun-up benignly, yet occurred in plasmas that ultimately disrupted, they are considered neither disruptive nor non-disruptive, and are excluded from the IRLM disruptivity studies. Similarly, a small number of discharges disrupt without an IRLM present, but did contain an IRLM 100 ms before the disruption or earlier. In these cases, it is not clear whether the IRLM indirectly caused the disruption or not, and therefore these cases are also excluded.

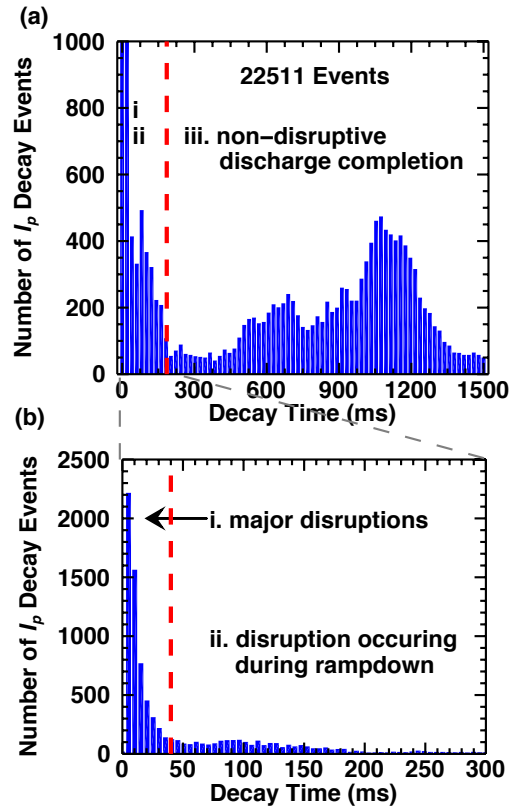


Figure 2. The distribution of plasma current decay time, roughly split into three populations. Panel (a) shows the non-disruptive discharges with decay times greater than 200 ms; panel (b) further distinguishes the remaining population into major disruptions (< 40 ms) and disruptions that occur during ramp-down. Note that the vertical axis on panel (a) is interrupted to better show the features in the distribution.

2.3. Detection of rotating modes of even m and $n=1$

Detection of a rotating mode is performed in two stages. For each shot, the signals from a pair of toroidally displaced outboard midplane magnetic probes are analyzed by the *newspec* Fourier analysis code [32], in search of $n=1$ activity. Genuine $n=1$ magnetohydrodynamic (MHD) activity is distinguished from $n=1$ noise by searching for both an $n=1$ amplitude sustained above a chosen threshold, as well as requiring the corresponding $n=1$ frequency to be "smooth". An adaptive threshold is used to accept both large amplitude, short duration modes, as well as small amplitude, long duration modes. Once detected, this activity is analyzed by a simplified version of the modal analysis *eigspec* code, based on stochastic subspace identification [31]. Here *eigspec* uses 9 outboard mid-plane and 1 inboard mid-plane Mirnov probes to isolate $n = 1$ and determine whether m is even or odd. Selecting modes of even m and $n = 1$ rejects $n = 1$ false positives due to 1/1 sawtooth activity, and other odd m and $n = 1$ activity. Modes

with $n=1$ and even m are predominantly $2/1$. Provided q_{95} is sufficiently high, they might in principle be $4/1$ or $6/1$ modes, but these modes are rare. Manual analysis of 20 automatically detected modes of even m and $n=1$ found only $2/1$ modes.

2.4. Detection of $n = 1$ locked modes

Locked modes are detected using difference pairs of the integrated external saddle loops (ESLDs). A toroidal array of six external saddle loops is available. Differencing of loops positioned 180° apart toroidally eliminates all $n = \text{even}$ modes, including the equilibrium fields. A least squares approach is then used to fit the $n = 1$ and $n = 3$ toroidal harmonics [32]. This approach assumes that the contributions of odd n with $n \geq 5$ are negligible.

Each pair-differenced signal is compensated for pickup of the non-axisymmetric coils, using a combination of analog and digital techniques. The accuracy of the coil compensations was assessed using vacuum shots from 2011-2014. Residual coil pickup peaks at ~ 3 G, but a conservative threshold of 5 G is chosen for identification of LMs to avoid false positives. Small LMs that produce signals less than 5 G are not considered in this work.

Analog integrators are known to add linear drifts to the saddle loop signals. In addition, $n = 1$ asymmetries in the plasma equilibrium can also produce background noise.

A simple yet robust algorithm was developed to subtract this background. The algorithm works on the principle that times exist during which it is impossible for a LM to exist, and the $n=1$ "locked mode signal" at those times must be zero. These times include the beginning and end of every shot, and times at which $m/n = \text{even}/1$ modes are known, from Mirnov probe analysis, to rotate too rapidly to be QSMs or LMs. As LMs cause a significant decrease in $\beta_N = \beta a B / I_p$ (as will be discussed in Section 7), the time when β_N is maximized is also highly unlikely to have a coincident LM, and therefore, this time is also used. A piecewise linear function with nodes at each identified "2/1 LM free" time is fit to each ESLD signal independently and subtracted to produce a signal with minimal effects from integrator drift and non-axisymmetric equilibrium pickup.

Fifty shots automatically identified to have LMs with $n = 1$ ESLD signals in excess of 5 G were manually analyzed. This analysis confirmed that in most cases the automatic identification was accurate, with a percentage of false positives for LMs *with* rotating precursors of $< 4\%$. The identification of locked modes *without* rotating precursors (born locked modes), on the other hand, exhibited a percentage of false positives $> 30\%$. Greater accuracy is achieved for

LMs with rotating precursors because the fast rotating precursor provides a LM free background subtraction just prior to locking. In addition, locked modes with rotating precursors require two subsequent events: the appearance of a rotating $m/n = \text{even}/1$ tearing mode followed by an $n = 1$ locked mode. Due to the high percentage of false positives in the identification of born LMs, they are not considered in this work but will be the topic of future work.

During the locked phase, no poloidal harmonic analysis is performed. It is assumed that the confirmed $m/n = \text{even}/1$ rotating mode present immediately before locking is likely a $2/1$ mode, and upon locking, the mode maintains its poloidal structure. In addition, it is assumed that the locked $n = 1$ signal measured by the ESLDs is predominantly due to the $2/1$ mode, such that this field measurement can be used to infer properties of the mode. A set of 63 disruptive IRLMs, occurring in plasmas with $|B_T| > 2$ T, were investigated using the 40 channel electron cyclotron emission (ECE) diagnostic [35] to validate these assumptions. Only plasmas with $|B_T| > 2$ T are considered to ensure that ECE channels cover a plasma region extending from the core through the last closed flux surface on the outboard midplane. Among these 63 IRLMs, 26 exhibited QSM characteristics, making full toroidal rotations, allowing the island O-point to be observed by the toroidally localized ECE diagnostic. In all 26 cases, a flattening of the electron temperature profile is evident at the $q = 2$ surface, and no surfaces with $q > 2$ show obvious profile flattening, suggesting that higher q modes are not present, or are too small to resolve by ECE channels separated by $\sim 1 - 2$ cm. As the gradient in the electron temperature tends to approach zero near the core, the presence or absence of a $1/1$ mode is difficult to conclude. Despite the $1/1$ mode existence being unknown, island widths derived from the radial field measured by the ESLDs, where the $n = 1$ signal is assumed to be a result of the $2/1$ mode only, agree to within ± 2 cm with the flattened T_e profiles as measured by ECE. We conclude that the assumptions that the locked mode is an $m = 2$, and that the signal in the ESLDs is predominantly due to the $2/1$, are accurate in the majority of cases. The minority of cases where this is not true are not expected to affect the statistical averages presented in this work.

2.5. Perturbed currents associated with the islands

The mode amplitudes will sometimes be reported in terms of the total perturbed current carried by the island δI . δI is a quantity that is local to the $q = 2$ surface, and its calculation accounts for toroidicity. The wire filament model used in [36] was shown to reproduce experimental magnetic signals well and was adapted for this calculation. An analytic version of

this model was developed which simulates the island current perturbation with helical wire filaments that trace out a torus of circular cross-section. The torus has the major and minor radii of the $q = 2$ surface informed by experimental EFIT MHD equilibrium reconstructions [37], which use magnetics signals and Motional Stark Effect measurements [38] to constrain the reconstruction. An analytic expression is found for δI as a function of the experimental measurement of B_R from the ESLDs, and R_0 and r_{q2} from EFIT reconstructions. The model and the resulting analytic expression are detailed in Appendix A.

3. Incidence of locking and global disruptivity on DIII-D

To motivate the importance of study of these $m/n = 2/1$ modes, figure 3 shows how often initially rotating 2/1 locked modes (IRLMs) occur in DIII-D plasmas. When considering all plasma discharges, 25% contain a 2/1 rotating NTM, 41% of which lock. IRLMs lead to a major disruption 76% of the time (using only the red and green portions of figure 3a, and the blue portion was excluded). Approximately 18% of all disruptions are a result of an IRLM, in good agreement with the $\sim 16.5\%$ reported on JET [16], and this statistic rises to 28% for shots with peak $\beta_N > 1.5$ (figure 3b). The blue slices show the number of IRLMs excluded from the disruptivity studies; the majority of which are shots that ramped down in plasma current while an IRLM still exists, and also include any IRLM that ceases to exist prior to a major disruption. The correlation between high β_N and rate of occurrence of IRLMs will be detailed in section 7.2.

While the vast majority of rotating NTMs lock before causing a disruption, there were approximately 23 instances of the rotating 2/1 mode growing large enough to disrupt before locking.

4. Timescales of locking

In this Section we present two timescales indicative of the time available for intervention before locking. These timescales are useful for disruption avoidance and mitigation techniques.

Figure 4 shows the duration of all rotating m -even, $n=1$ modes that locked. A broad peak exists between 50 and 400 ms. The rotating duration can depend on several different factors, such as the plasma rotation frequency, applied Neutral Beam Injection (NBI) torque, the island moment of inertia, and viscous torques. The spread of values gives an indication of the time available to prevent locking, if an intervention is triggered upon rotating mode detection.

The time taken for a mode rotating at 2 kHz

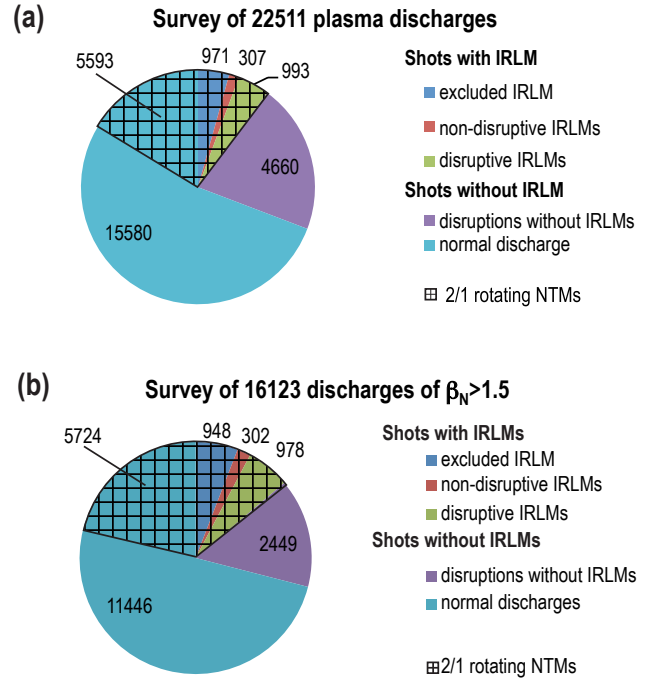


Figure 3. (a) Color pie chart surveying all plasma discharges, showing the fraction of discharges with disrupting and non-disrupting initially rotating locked modes (IRLMs), as well as disruptions without IRLMs. Overplotted as a hatched region are the discharges with rotating 2/1 NTMs. (b) Same pie chart as (a), but for discharges with peak $\beta_N > 1.5$. Note that there is a slight overlap of 23 shots between the hatched rotating NTM and the purple disruption regions.

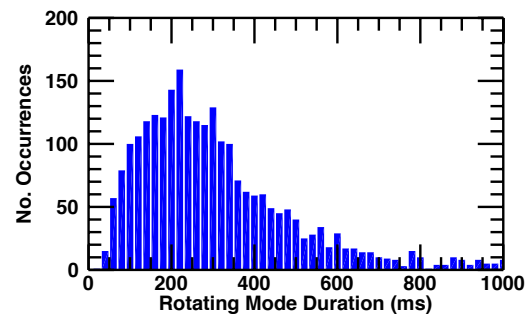


Figure 4. Histogram distribution of duration of rotating precursors (from mode onset to locking).

to slow down and lock is referred to here as the slow-down time. The threshold of 2 kHz was chosen empirically, as modes that decelerate to this frequency are often observed to lock. It is probable that at this frequency, the decelerating wall torque is stronger than the accelerating viscous torque, and causes the mode to lock. Figure 5a shows the majority of slow-down times between 5 and 45 ms; this is an indication of the time

available to prevent locking if an operational 'alarm' is set at 2 kHz.

Figure 5b shows that modes which experience a larger wall torque generally slow down quicker than those with smaller wall torques. While 66% of modes rotating at 2 kHz lock in a time comprised between 5 and 45 ms, the most frequent slow-down time is about 17 ± 10 ms, an indication of the time available to avoid mode locking. At low electromagnetic torque, the spread of slow-down times in figure 5b suggests that other effects, such as the NBI torque, also become important.

The electromagnetic torque between the rotating mode and the wall is expressed as follows [4]

$$T_{\phi,wall} = \frac{mR_0(2\pi r_s B_{rs})^2}{n\mu_0} \frac{(\omega\tau_w)(r_{s+}/r_w)^{2m}}{1 + (\omega\tau_w)^2[1 - (r_{s+}/r_w)^{2m}]^2}$$

where m and n are the poloidal and toroidal harmonics, r_s is the minor radius of the $q = 2$ surface, $r_{s+} = r_s + w/2$ with w being the island width, B_{rs} is the perturbed radial field at the $q = 2$ surface, r_w is the minor radius of the resistive wall, and ω is the rotation frequency of the NTM co-rotating with the plasma. This form of the electromagnetic torque comes from a cylindrical approximation.

5. Time between locking and disruption

The survival time is defined as the duration of a disruptive IRLM between locking and disruption. Figure 6 is a histogram of the survival times of all disruptive IRLMs. Two groups can be observed, peaking at less than 60 ms and at 270 ms. The first group consists of 80 large rotating modes that lock and disrupt almost immediately, as opposed to the latter spread of LMs that reach a meta-stable state before disrupting. These short-lived modes, though dangerous and undesirable, could not be studied in detail as necessary equilibrium data do not exist. Future work will attempt to characterize these modes.

While 75% of the population (excluding transient modes) survive between 150 to 1010 ms, the most frequent survival time is 270 ± 60 ms, an indication of time available to avoid disruption when a mode locks.

Gaining predictive capability over how long a disruptive locked mode is expected to survive might guide the best course of action to take, e.g. whether to stabilize the mode, or directly deploy disruption mitigation techniques.

Figure 7 shows the survival time plotted against the poloidal beta β_p , the distance d_{edge} , and the perturbed island current δI . d_{edge} is a quantity that measures the shortest distance between the island separatrix and the unperturbed plasma separatrix: $d_{edge} \equiv a - (r_{q2} + w/2)$ where a is the minor radius

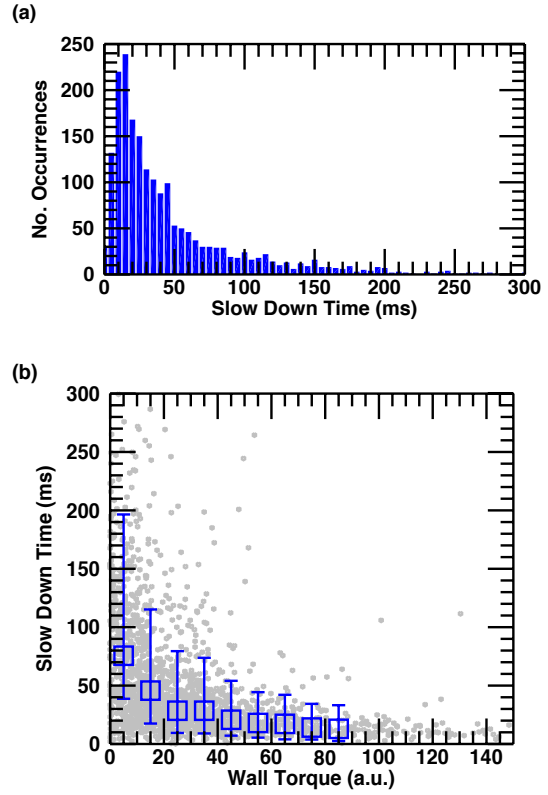


Figure 5. (a) The time taken for a rotating $m/n = 2/1$ mode to slow from 2 kHz to locked, as measured by *eigspec* and ESLDs respectively. (b) A correlation is observed between the measured slow-down time and electromagnetic torque between the mode and the wall. The points and error bars are the median and 25th and 75th percentiles respectively. Note that about 5% of the events lie beyond 300 ms, and are not plotted (in either panel).

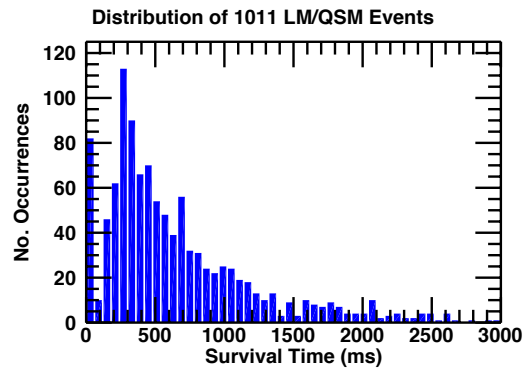


Figure 6. A histogram of the survival time, defined as the duration of a locked mode that ended in a disruption. Less than 2% of events survive for more 3000 ms.

of the unperturbed plasma separatrix, r_{q2} is the minor radius of the $q = 2$ surface, and w is the island width.

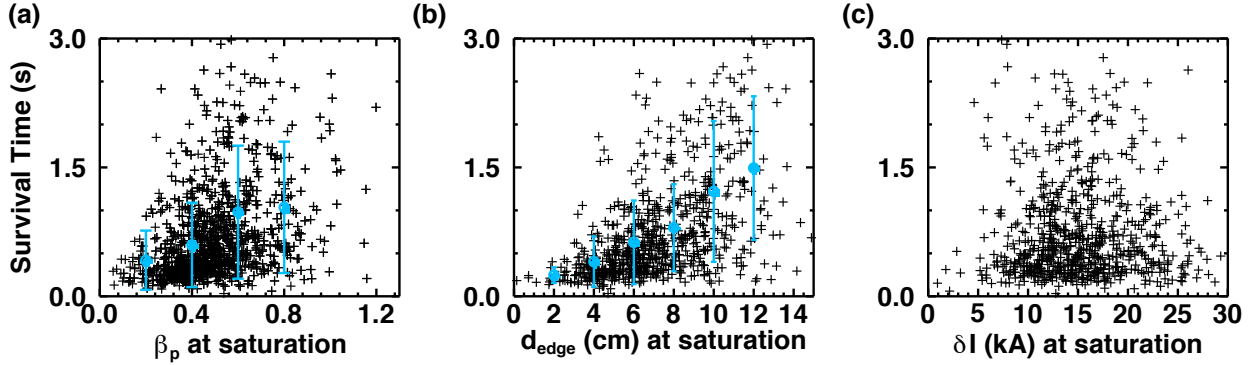


Figure 7. Survival time shows some dependence on (a) β_p and (b) d_{edge} . (c) No correlation is found with δI or similarly with the island width w (see table 1).

Parameter	Correlation with t_s
d_{edge}	0.47
ρ_{q2}	-0.42
l_i/q_{95}	-0.39
q_{95}	0.36
β_p	0.34
$dq/dr(r_{q2})$	-0.15
l_i	-0.11
w	0.10
δI	-0.01

Table 1. Correlations of various parameters with the IRLM survival time t_s . The parameters are ordered in the table by the absolute value of their correlation coefficient. Negative correlation means that a linear relationship with a negative slope exists between the parameters.

In figure 7, the survival time shows some correlation with β_p and d_{edge} , but not with δI . The correlation coefficients for these, and other parameters are listed in table 1. The lack of correlation between survival time and δI is consistent with the lack of correlation with the island width w . This suggests that large islands will not necessarily disrupt quickly, but islands which extend near to the unperturbed separatrix (i.e. islands with small d_{edge}) tend to disrupt quickly. The correlation of d_{edge} with survival time suggests that it is pertinent to the physics of the thermal quench. Other works have found that parameters similar to d_{edge} appear to cause the onset of the thermal quench [39, 40, 41] (see section 9 for details).

The best correlations in the table are considered moderate (i.e. moderate correlations are in the range $r_c = [0.4, 0.6]$, where r_c is the correlation coefficient). The correlations in table 1 do not provide significant predictive capability. A macroscopic timescale like the survival time likely depends on many variables, and on the nonlinear evolution of the plasma under the influence of the locked mode.

6. Mode amplitude and phase evolution

6.1. Distributions of IRLM toroidal phase at locking

As a rotating $n = 1$ mode is slowing down and about to lock, it tends to align with existing $n = 1$ fields. In most cases, this will be the residual error field, defined as the vector sum of the intrinsic error field and the applied $n = 1$ error field correction. Figure 8 shows a histogram of all locked mode phase data, normalized by mode duration and total number of modes in the given set: each mode contributes a total of $100/N$, where N is the total number of disruptive or non-disruptive modes; and further normalized by binsize of 5 degrees. A clear $n = 1$ distribution is observed in figure 8a (left-hand helicity discharges), with a peak at $\sim 125^\circ$ for disruptive modes and $\sim 110^\circ$ for non-disruptive modes. Figure 8b shows right-hand helicity discharges. The disruptive distribution shows an $n = 1$ component, though an $n = 2$ component is also clearly visible. The non-disruptive distribution shows a strong $n = 2$ component. The presence of $n = 2$ might be due to occurrences of both over and under correction of the intrinsic error field. Alternatively, the $n = 2$ distribution might arise from the presence of both locked and quasi-stationary modes. Locked modes are expected to align with the residual, whereas quasi-stationary modes are expected to move quickly past the residual, spending the most time in the anti-aligned phase. Similar analysis on subsets of these data shows consistent results, suggesting that these distributions are not specific to a certain experimental campaign.

The intrinsic $n = 1$ error field in DIII-D has been characterized by in vessel apparatuses [42, 43] and the errors attributed to poloidal field coil misalignments and ellipticity, and the toroidal field buswork. It is found that the intrinsic error is well parameterized by the plasma current I_p and the toroidal field B_T ; "standard error field correction" in the DIII-D plasma control system calculates $n = 1$ correction fields based

on these. The majority of DIII-D plasmas are run with I_p in the counter-clockwise direction and B_T in the clockwise direction when viewed from above, referred to as the "normal" directions. Taking ranges for I_p and B_T expected to encompass the majority of left-hand helicity discharges (i.e. $I_p = 0.8$ to 1.5 MA and $B_T = -1$ to -2.1 T), the standard error field correction algorithm applies correction fields between 196° and 250° . The preferential locking angles shown in figure 8a might be due to a *residual* EF, resulting from the vector addition of the intrinsic EF and an imperfect correction field.

Figures 8c-d show how residual fields can arise from changing intrinsic and/or correction fields. Figures 8e-f illustrate how the distributions in 8a-b might look if the residual is reproducible, or not. In the former case, a narrow, peaked distribution is expected, whereas in the latter case, a broad, flat distribution is expected. This might explain the distributions in figures 8a-b. In addition, quasi-stationary modes are also present in these data, and contribute to the broadening.

6.2. Change in $n = 1$ field at locking and growth before disruption

Figure 9 shows the change in mode width as the NTM slows from rotating at $f = 2$ kHz to 50 ms after locking. To within the ± 2 cm errors on the width estimate from magnetics, a significant growth or decay at locking is not observed for the majority of modes. Only $\sim 10\%$ of locked modes appear above the top diagonal dashed line, indicating a growth at locking beyond error.

It has been observed across the database that the radial field B_R measured by the ESLDs tends to grow before disruption. This growth is distinct from the dynamics of the locking process, as it often occurs hundreds of milliseconds after locking. Figure 10a shows the B_R behavior before disruption for five randomly chosen disruptive IRLMs. A general period of growth occurs between ~ 100 and 5 ms prior to the disruption, followed by a sharp rise in B_R coincident with the thermal quench (marked by the transient rise in I_p before the current quench). Although interesting in its own right, we will not investigate the details of the B_R spike during the thermal quench, as we are interested in the dynamics leading up to the thermal quench.

Histograms in radial field B_R are plotted in figure 10b, at times before disruption, to study the average evolution. The B_R field in a single case often follows a complicated trajectory, as evidenced by figure 10a, but these histograms reveal global trends. In Figure 10b, the centers of the distributions shift to higher values of B_R as the disruption is approached. The median is chosen to be the representative point in the

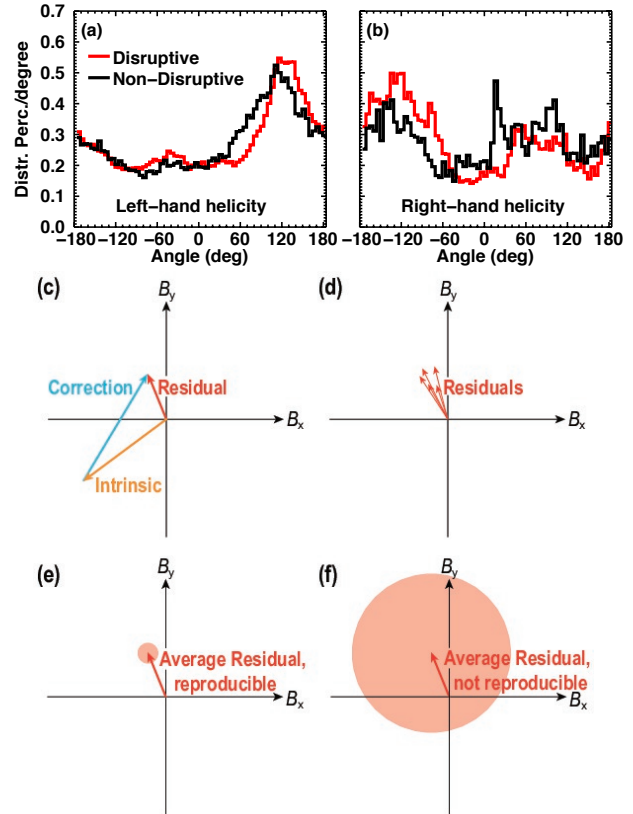


Figure 8. The normalized phase distribution of all locked modes. Each mode contributes a total of $100/N$ across all bins (N is number of disruptive or non-disruptive IRLMs). A binsize of 5 degrees was chosen as a compromise between being large enough to have sufficient statistics in one bin and fine enough to show features of interest. The angle is where the radial field is largest and outward on the outboard midplane. (a) Left-hand helicity (i.e. normal I_p and B_T , or both reversed) with 980 disruptive and 1029 non-disruptive IRLMs. (b) Right-hand helicity plasma discharges (i.e. either I_p or B_T reversed). Only 130 disruptive and 204 non-disruptive IRLMs here. (c-f) Illustrations to explain distributions. (c) The residual EF is the difference between the intrinsic EF and the applied correction. (d) Due to changes in the intrinsic and/or the correction, the residual EF can change. (e) An average residual can be defined by averaging over several shots and times. A small standard deviation in its amplitude and phase (illustrated by the small circle) are indicative of high reproducibility of the residual EF. In that case, a narrow distribution is expected in Fig.a-c. (f) In the opposite limit, the residual EF phasor can point to any quadrant, and a broad, flat distribution is expected

analysis that follows. The median is the point on the distribution which divides the area under the curve equally.

The median is plotted in figure 10c as a function of time (note the y -axis is logarithmic). The median major radial field is about 7 G at saturation (i.e. 50 ms after locking). Later in the lifetime of the mode, and approximately 50 ms prior to the disruption, the median grows exponentially from the saturated value, reaching a final value of > 11 G at ~ 5 ms before the

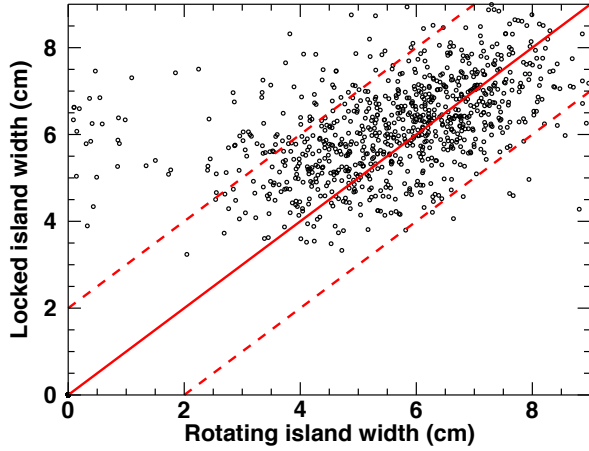


Figure 9. The mode width before and after locking, as calculated from the Mirnov probe array and ESLD measurements respectively. The rotating mode width is evaluated when mode rotation reaches 2 kHz; locked mode width evaluated at 50 ms after locking to allow decay of shielding currents in the wall. The solid line shows where the widths are equal, while the dashed red lines quantify the conservative ± 2 cm error bar on the island width estimates.

disruption. This time is approximately coincident with the onset of the thermal quench. From the slope of the line in figure 10c, an exponential e -folding time for B_R in the range $\tau_g = [80, 250]$ ms is found.

The present analysis is not sufficient to discern between possible sources of this increased B_R . Out of the 26 IRLMs for which $2/1$ modes can be clearly seen on ECE (see discussion in section 2.4), less than 10 of these provide a view of the island O-point during the disruption. One such case is shot 157247 shown in figure 11 which disrupted at 3723 ms. A significant flattening of the T_e profile is seen at each time slice, confirming that a $2/1$ island with $w > 5$ cm is present. The solid horizontal bars show the calculated island position (from EFIT) and width (derived from δI , see Appendix B). The solid line in figure 11b shows the toroidal location of the island O-point on the outboard side in the midplane, and it is seen to intersect the location of the ECE diagnostic (dashed horizontal) at $t \approx 3660$ ms. The vertical dashed lines show the toroidal alignment of the O-point with the ECE for each timeslice. Note that the worst toroidal alignment occurs for $\phi_{LM} = -99^\circ$, where the X-point is aligned with the ECE. The horizontal bar at 3710 ms (green in online version) looks to over predict the island width by ~ 3 cm, though the island toroidal alignment with the ECE is intermediate between the O and X-points, where the flattened region is expected to be smaller. EFIT data do not exist for the last two timeslices.

In all shots where magnetics predict O-point alignment with ECE during the disruption, a clear

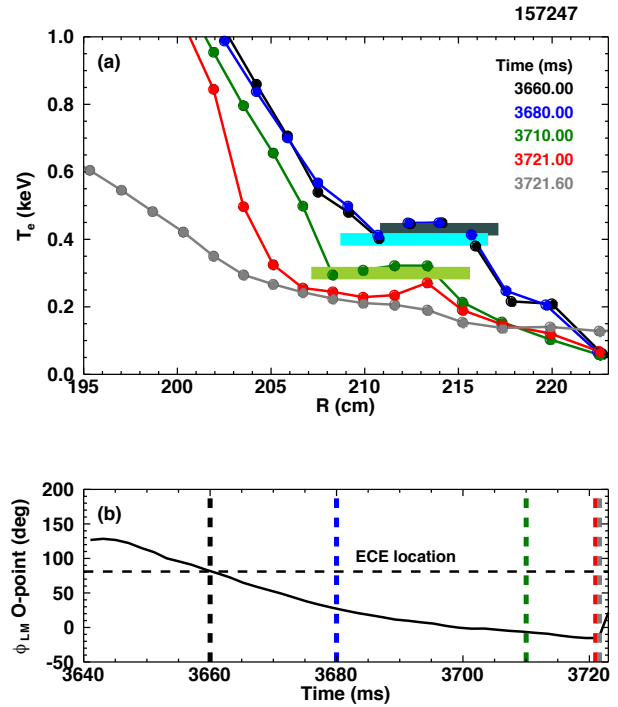


Figure 11. (a) T_e profiles from ECE prior to an IRLM disruption show a clear flattening at the $q = 2$ surface. Horizontal bars show the automated estimation of island position and width (note the vertical position of the bars is chosen for visual purposes only). (b) The toroidal position of the island O-point on the outboard side in the midplane. The horizontal dashed line shows the toroidal location of the ECE diagnostic, and the vertical dashed lines show the time slices from (a).

flattening of the T_e profile like that shown in figure 11 is observed. We conclude that the assumption of the presence of an $m = 2$ island during the disruption is accurate, and in the shots where ECE data are available, the predicted island widths are reasonable.

If we assume that the increase in the $n = 1$ field measured by the ESLDs is due to growth of the $2/1$ island, we can estimate how much the island width would increase. We assume a constant B_T , R , and $dq/dr|_{q2}$ during the ~ 100 ms of growth, where the field increases from 7 to 11 G. Therefore, from equation 16, we expect the island width to increase by $\sqrt{11/7} \approx 1.25$. With an average saturated width for disruptive islands of ~ 6 cm (this will be shown in section 8), a disruptive island would be expected to grow ~ 1.5 cm during the exponential growth. With a channel spacing of 1-2 cm for ECE measurements, and with less than 10 disruptive IRLMs whose O-points are well aligned with the ECE diagnostic during the disruption, validating this small change in island width would be difficult.

As the poloidal harmonic of this exponentially growing $n = 1$ field is unknown, in principle it is possible that the $2/1$ island is unchanging, while

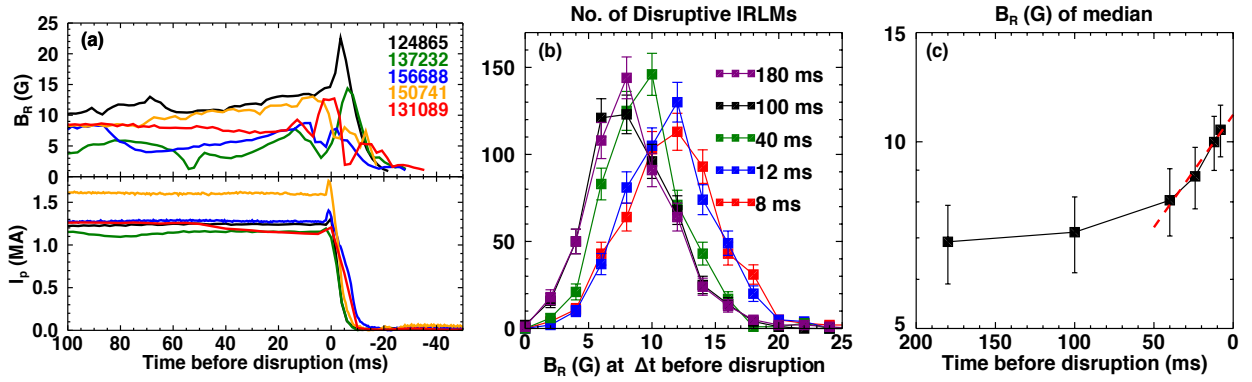


Figure 10. (a) B_R and I_p traces from five randomly chosen disruptive IRLMs. (b) Histograms of B_R for all disruptive IRLMs at times approaching disruption. (c) The median of the histograms in (b) shows exponential growth within 50 ms of the disruption with an e -folding time in the range $\tau_g = [80, 250]$ ms.

an $m = 1$ or $m = 3$ instability is appearing and growing. Coupling of the $2/1$ and $3/1$ modes has been observed on ASDEX-Upgrade [44] and investigated in numerical studies [45], while coupling of the $2/1$ and $m/n = 1/1$ has been observed on TEXTOR [46], the RTP Tokamak [14], and studied in simulations [41]. Although $m = 4$ might be a candidate for this growth in some shots, it will be shown in section 8 that more than half of the disruptive discharges have $q_{95} < 4$, so it could only explain a minority of cases. Similarly, out of 13 IRLMs that occur in plasmas with $q_{95} < 3$, at least 7 show a clear disruptive growth, in which the $m = 2$ or $m = 1$ modes are the only candidates for this growth.

Note that although we have chosen to characterize the final disruptive growth here, a single mode might undergo multiple growths and minor disruptions, as shown in figure 1.

7. Interdependence of locked modes and β

7.1. Effect of locked mode on β and equilibrium

A common sign of the existence of a LM is a reduction in plasma β . Here we investigate $\beta_N = \beta(aB/I_p)$ as it has been shown to affect NTM onset thresholds [47] (a is the plasma minor radius and B is usually taken to be the toroidal field on axis).

Figure 12a shows β_N at locking as a function of β_N at mode onset. Raw data for disruptive modes are shown in red and purple. The purple disruptive modes are preceded by an earlier LM, while the red are not. The majority of the red points are observed to lie below the dashed diagonal. This observation is reiterated by the light blue points, showing the average and standard deviation also lying predominantly below the diagonal, meaning that β_N decreases from NTM onset to locking.

Notice that a significant population of purple points lie above the dashed line for β_N at rotating onset

< 1.5 . The rotating phase of these IRLMs begins with frequency $f = 0$ (locked), and then they spin up. In these cases, β_N has suffered a large degradation from the previous locked mode. In most of these cases, the β_N at the following locking is greater than the degraded β_N at the time of spin up, and therefore the points lie above the dashed line.

The light blue and black averages from figure 12a are replotted in figures 12b and 12c in the form of percent changes in β_N at each stage, relative to the β_N at rotating onset. These plots show how β_N changes from the rotating onset to locking, to β_N saturation, and to mode termination. The time of β_N saturation is taken to be 200 ms after locking (found empirically, in approximate agreement with twice the typical DIII-D energy confinement time, $\tau_E \approx 100$ ms), and the time of mode termination is taken to be 50 ms before disruption or disappearance of the mode. Except for the initial phase with β_N at rotating onset < 1.5 , a continuous decrease in β_N is observed during successive phases of the IRLM.

On average, the disruptive modes cause a larger degradation of β_N than non-disruptive modes during all three phases. For β_N at rotating onset > 1.6 , disruptive modes cause 20-50% reduction during the rotating phase, 50-70% reduction by β_N saturation, and 50-80% reduction within 50 ms of the disruption. Of course a further, complete loss of β_N occurs at disruption (not shown).

With the reduction in β_N in figure 12, and assuming constant I_p and B_T (which is accurate for most modes occurring during the I_p flattop), a similar reduction in $\beta_p = \langle p \rangle / (B_\theta^2 / 2\mu_0)$ is expected as well. The reduction in β_p causes a reduction in the Shafranov shift. Figure 13 shows the linear dependence of R_0 on β_p during the first 200 ms after locking. A linear fit to the disruptive data provides a shift ratio of $\Delta R_0 / \Delta \beta_p \approx 4$ cm. Most modes reduce the Shafranov

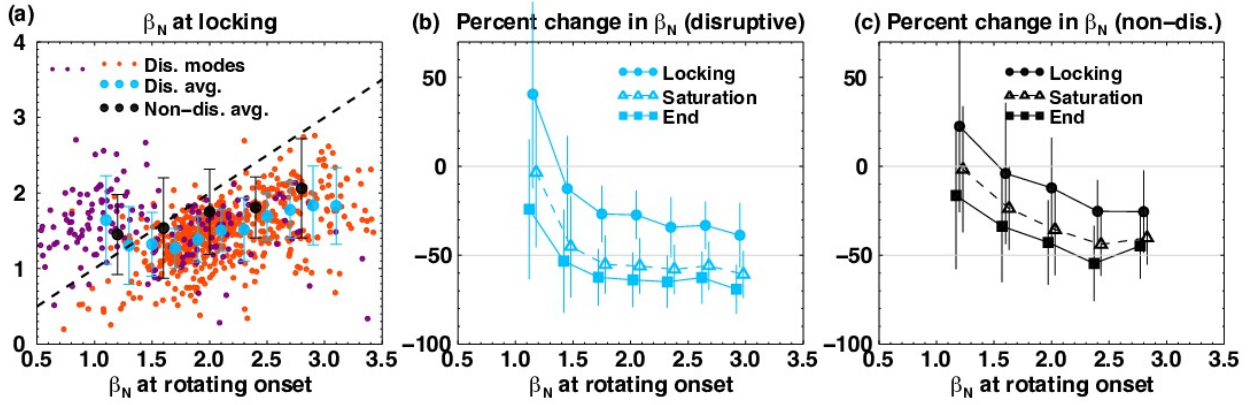


Figure 12. (a) The time evolution of β_N between onset of the rotating mode, and mode locking. The blue and black points show the average and standard deviation of the disruptive (red and purple) and non-disruptive (raw data not shown) populations. The purple disruptive IRLMs are preceded by another LM (red are not). (b) The percent change in β_N during each phase of disruptive IRLMs, as compared with the β_N at time of rotating onset. (c) Same as (b), but for non-disruptive IRLMs.

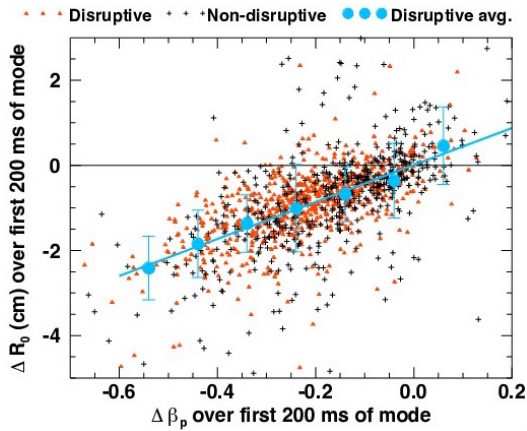


Figure 13. Both disruptive and non-disruptive modes show a linear dependence with $\Delta R_0/\Delta \beta_p \sim 4$ cm. A number of outliers are produced in the non-disruptive population by significant changes of plasma shape (e.g. diverted to wall-limited plasma).

shift by 0-3 cm. This reduction of the 1/0 shaping reduces toroidal coupling of the 1/1 and 2/1 modes, the 2/1 and 3/1 modes, and other m/n and $(m+1)/n$ mode combinations. The larger scatter in the non-disruptive population can be explained at least in part by significant shape changes, such as the transition from diverted to wall limited. For this reason, the linear fit is performed only on the disruptive data.

7.2. Effect of β on the saturated width, IRLM rate of occurrence, and disruptivity

As NTMs are the result of helical perturbations to the bootstrap current [10], we expect the island width to depend on terms that drive the bootstrap current. The Modified Rutherford Equation (MRE) has been shown in previous works to describe 3/2 [6, 48] as well as 2/1

[49, 50] tearing mode saturation well. The saturated modes of interest here have an average width $w \approx 6$ cm and a standard deviation $\sigma \approx 2$ cm. Being that small island terms in the MRE start to become small for $w > 2$ cm (assuming $w_{pol} \approx 2$ cm [10]), small island effects are ignored. A steady state expression of the MRE (i.e. $dw/dt \rightarrow 0$) is given as follows,

$$0 = r\Delta'(w) + \alpha\epsilon^{1/2} \frac{L_q}{L_{pe}} \beta_{pe} \frac{r}{w} + 4 \left(\frac{w_v}{w} \right)^2 \quad (1)$$

where $\Delta'(w)$ is the classical stability index, α is an *ad hoc* accounting for the stabilizing effect of field curvature ($\alpha \approx 0.75$ for typical DIII-D parameters), $\epsilon = r/R$ is the local inverse aspect ratio, $L_q = q/(dq/dr)$ is the length scale of the safety factor profile, $L_{pe} = -p_e/(dp_e/dr)$ is the length scale of the electron pressure profile ($L_{pe} > 0$ as defined), β_{pe} is the electron poloidal beta, and w_v is the vacuum island width driven by the error field ($w_v \sim 1$ cm in DIII-D). Note that usually a cosine term appears on the term involving w_v [51], but it is set to unity here, which assumes the most destabilizing alignment of the locked mode with the error field.

We take $\Delta'(w)$ to be of the form $\Delta'(w) = C_0/r - C_1 w/r^2$ [8]. With this definition of $\Delta'(w)$, equation 1 is a nontrivial cubic equation in w . However, an approximate solution was found by approximating $(w_v/w)^2 \approx aw_v/w - b$ (with $a = 0.45$, $b = 0.045$, found to be accurate to within 15% over the domain $w_v/w = [0.12, 0.3]$). The resulting equation is quadratic, of straightforward solution. The approximate saturated width expression is given by,

$$\frac{2w_{sat}}{r} = \left(\frac{C_0 - 4b}{C_1} \right) + \left[\left(\frac{C_0 - 4b}{C_1} \right)^2 + \frac{4}{C_1} \left(\alpha\epsilon^{1/2} \frac{L_q}{L_{pe}} \beta_p + 4a \frac{w_v}{r} \right) \right]^{1/2} \quad (2)$$

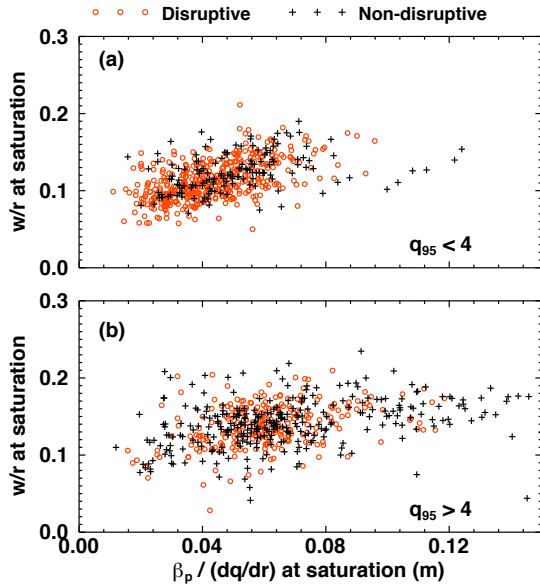


Figure 14. (a) The normalized island width at saturation as a function of $\beta_p/(dq/dr)$ for discharges with $q_{95} < 4$. (b) Same as (a) for discharges with $q_{95} > 4$. Only islands with $w < 9$ cm are shown here.

The data in figure 14 show the normalized island width as a function of $\beta_p/(dq/dr)$. The parameters L_p and $\Delta'(w)$ are difficult to acquire with automated analysis, and therefore are not available in the database. Therefore, a direct fitting of equation 2 is not appropriate, but the conclusion that w_{sat}/r increases with $\beta_p/(dq/dr)$ is evident. A correlation of $r_c = 0.55$ is found between w_{sat}/r and $\beta_p/(dq/dr)$ for plasmas with $q_{95} < 4$. Plasmas with $q_{95} > 4$ show a weaker correlation with $r_c = 0.36$. This correlation suggests that locked modes in DIII-D are driven at least in part by the bootstrap current.

A one dimensional study of IRLM frequency (or prevalence) versus β_N suggests that intermediate β_N shots are the most prone to IRLMs, as shown in figure 15. The fraction of shots containing an IRLM increases with β_N up to 2.75.

The fraction of shots with IRLMs decreases significantly for $\beta_N \geq 4.5$. A manual investigation of the 38 shots in this bin reveals that these discharges often have (1) $q_{95} \geq 5$, or (2) high neutral beam torques of $T \approx 6$ Nm, or both. In both cases, a low occurrence of IRLMs might be expected due to a weak wall torque: (1) the $q = 2$ surface is far from the wall in discharges with high q_{95} , and (2) shots with high injected torque likely exhibit high plasma rotation, in a regime where the wall torque goes like ω^{-1} . A three-dimensional analysis of IRLM frequency versus β_N , ρ_{q2} , and NBI torque might be more informative. These data are not populated for all shots in the database, so this analysis is reserved for future work.

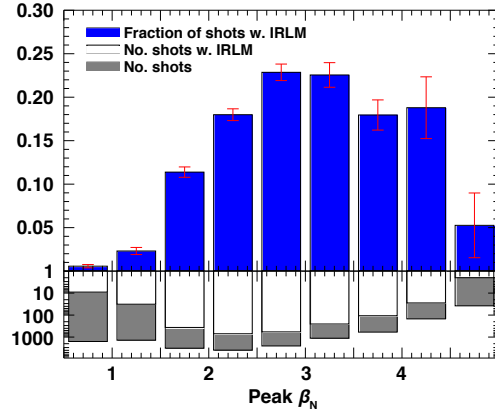


Figure 15. The shot-wise rate of occurrence of IRLMs (no. of shots with IRLMs / total no. of shots) as a function of the maximum β_N achieved during the shot. Blue bars (on top) are formed by the quotient of the white and gray (on bottom). Note the logarithmic axis for the lower axis.

The IRLM disruptivity as a function of β_N and q_{95} is plotted in figure 16. The IRLM disruptivity is defined as the "number of shots with disruptive IRLMs" divided by the "number of shots with IRLMs". Considering IRLM disruptivity as a function of β_N only, the histogram at the right of figure 16a shows a peaked distribution, with the highest values for $\beta_N \sim 1.5 - 3$. Similar results were obtained for the global disruptivity as a function of β_N at NSTX [17] (study not limited to locked modes, and normalized by the amount of time spent at the given β_N value). Reduced locked mode disruptivity at high β_N was also observed at MAST [29].

The IRLM disruptivity dependence on β_N can be explained in part by the reduced number of discharges with $q_{95} < 3.5$ with high β_N . To see this, we bin the data in figure 16a into five β_N windows, denoted $\beta_0, \beta_1, \dots, \beta_4$. First, note that figure 16b shows a general decrease in IRLM disruptivity as q_{95} is increased, across all β_N windows. Next, figure 16c shows the percent distribution of q_{95} values in each of these β_N windows. The two highest values of β_N (purple and green) have the lowest percentage of discharges with $q_{95} < 3.5$, and the highest percentage of discharges for q_{95} between 4.5 and 5. This distribution of q_{95} reduces the number of disruptive discharges, with the net result that the higher β_N discharges appear less disruptive.

As q_{95} is shown here to affect IRLM disruptivity, fixing q_{95} removes one variable, and allows us to more closely inspect the dependence of IRLM disruptivity on β_N . Figure 16b shows IRLM disruptivity across five windows in β_N (denoted by color), for five values of q_{95} (separated by vertical gray lines). In all q_{95} windows, there is either no significant dependence on β_N , or a lower IRLM disruptivity at higher β_N , particularly in

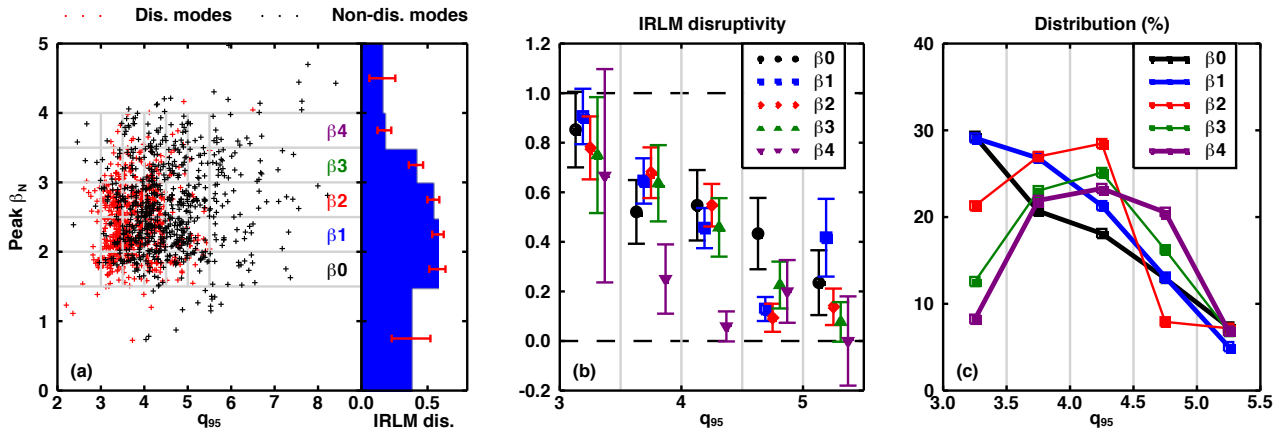


Figure 16. (a) The raw data for the highest achieved β_N as a function of q_{95} . The histogram on the right shows the one-dimensional IRLM disruptivity as a function of peak β_N . Windows in β are labeled, and the binning for figures (b) and (c) are shown in gray. (b) IRLM disruptivity as a function of q_{95} for the binned data in (a). (c) The distribution of each β_N bin in q_{95} in percent.

the window $3.5 < q_{95} < 4.5$. Although larger islands are expected at higher β_N , it will be shown in the next section that IRLM disruptivity depends very weakly on island width (refer to figure 18), and therefore it also depends weakly on β_N . It should be noted that only q_{95} is fixed here. Other parameters that are correlated with β_N (e.g. NBI torque, ion and electron temperatures, and possibly others) are not fixed, and might affect the apparent IRLM disruptivity scaling.

8. IRLM disruptivity

8.1. Decoupling the effects of ρ_{q2} , q_{95} , and l_i on IRLM disruptivity

Figure 17a shows the normalized radius of the $q = 2$ surface ρ_{q2} and q_{95} at the mode end, defined here to be 100 ms prior to the termination of the mode. The data are from equilibrium reconstructions constrained by both the external magnetics, and the Motional Stark Effect (MSE) diagnostic. On the right and below figure 17a are histograms of IRLM disruptivity as a function of ρ_{q2} and q_{95} respectively. The q_{95} histogram shows the expected result that lower q_{95} is more disruptive, as was also seen in figure 16b. The total disruptivity (i.e. not limited to IRLM disruptions) is observed to increase as q_{95} is decreased in DIII-D [19]. This is in agreement with, but not limited to, observations from JET [15], NSTX [17], and MAST [29]. The histogram in ρ_{q2} has a qualitatively similar shape, with the highest IRLM disruptivity at large ρ_{q2} , and the lowest at small ρ_{q2} .

The raw data show an expected correlation between ρ_{q2} and q_{95} . In a circular cross-section,

cylindrical plasma, q_{95} can be defined as follows,

$$q_{95} = \frac{2}{\rho_{q2}^2} \left[1 + \frac{I_{out}}{I_{enc}} \right]^{-1} \quad (3)$$

where I_{enc} is the total toroidal current enclosed by the $q = 2$ surface, and I_{out} is the total toroidal current outside of the $q = 2$ surface. Note that the quotient I_{out}/I_{enc} behaves similar to the inverse plasma internal inductance l_i^{-1} : when I_{out}/I_{enc} is large, l_i is small, and vice versa. The lack of one-to-one relationship between ρ_{q2} and q_{95} in the raw data of figure 17a may therefore be attributed in part to variations in I_{out}/I_{enc} . In toroidal geometry, plasma shaping may also introduce variation in the relationship between q_{95} and ρ_{q2} .

Empirically, we find a high correlation ($r_c = 0.87$) between l_i/q_{95} and ρ_{q2} , suggesting a relationship of the form,

$$l_i/q_{95} = \alpha \rho_{q2} + c \quad (4)$$

where $\alpha = 0.67 \pm 0.01$, and $c = -0.23 \pm 0.01$. This equation suggests that ρ_{q2} specifies l_i/q_{95} , or vice versa. We begin by studying the effects of q_{95} , l_i , and ρ_{q2} on IRLM disruptivity individually. Then, we investigate IRLM disruptivity as a function of ρ_{q2} and l_i/q_{95} , which despite the high correlation between the two, reveals that l_i/q_{95} distinguishes disruptive IRLMs better than ρ_{q2} .

First, to decouple the effect of q_{95} and ρ_{q2} on IRLM disruptivity, we fix one and study the dependence on the other in figure 17. We approximately fix ρ_{q2} by considering only data that lie in small windows of ρ_{q2} denoted ρ_1 , ρ_2 , ρ_3 , and ρ_4 (ρ_4 covers a relatively large window in ρ_{q2} as data become sparse, but IRLM disruptivity appears constant throughout the window). IRLM disruptivity as a function of q_{95} in the ρ_{q2} windows is shown in

figure 17b. Neither the trace corresponding to ρ_1 nor ρ_2 show a significant trend with IRLM disruptivity beyond error. Both ρ_3 and ρ_4 show a possible decrease in IRLM disruptivity for $q_{95} > 5.5$, but appear constant for $q_{95} < 5.5$.

The same study is performed on ρ_{q2} by choosing windows in q_{95} (or safety factor) denoted SF1, SF2, and SF3 (figure 17c). The three safety factor windows agree within statistical error on an increasing linear trend, with $< 20\%$ IRLM disruptivity for $\rho_{q2} < 0.7$, and $> 80\%$ for $\rho_{q2} > 0.85$.

From equation 4, we see that fixing ρ_{q2} and varying q_{95} (as in figure 17b) implies a variation of l_i as well. The weak or absent trend in IRLM disruptivity as a function of q_{95} might be explained by competing effects of q_{95} and l_i .

Similarly, equation 4 shows that fixing q_{95} and varying ρ_{q2} (as in figure 17c) also implies varying l_i . The strong dependence of IRLM disruptivity on ρ_{q2} thus suggests that either ρ_{q2} , l_i , or both have a strong effect on IRLM disruptivity.

To help isolate the individual effects of ρ_{q2} , q_{95} , and l_i , we compare how well they separate disruptive and non-disruptive IRLMs single-handedly.

In order to quantify separation of the distributions in one-dimension, we employ the Bhattacharyya Coefficient (BC) [52]. This coefficient was developed to measure the amount of overlap between two statistical distributions, and is commonly used in image processing, particularly for measuring overlap of color histograms for pattern recognition and target tracking [53]. For two discrete probability distributions p and q parameterized by x , the Bhattacharyya Coefficient is given by,

$$BC(p, q) = \sum_{x \in X} \sqrt{p(x)q(x)} \quad (5)$$

The BC metric varies over the range $0 \leq BC(p, q) \leq 1$, where a value of 1 indicates that p and q are identical and perfectly overlapping. A value of 0 implies they are completely distinct (no overlap)

Figure 18 shows the 1D separation of disruptive and non-disruptive modes for six parameters at 100 ms before mode termination, and reports the BC value for each. Of the three interdependent parameters (i.e. ρ_{q2} , q_{95} , and l_i), ρ_{q2} is observed both visually, and by the $BC = 0.70$ value to best separate the two populations. The parameters q_{95} and l_i produce less separation with coefficients of $BC = 0.85$ and $BC = 0.88$ respectively.

Disruptivity is found to scale strongly with plasma shaping in NSTX [17]. The effects of shaping on IRLM disruptivity in DIII-D will be included in a future work.

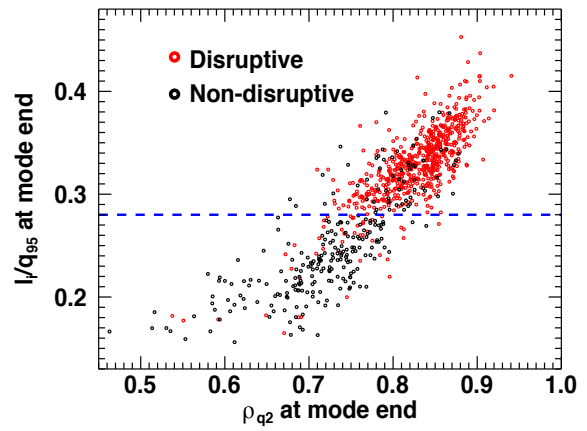


Figure 19. Investigation of l_i/q_{95} versus ρ_{q2} across all disruptive and non-disruptive IRLMs. Mode end is 100 ms prior to mode termination. The high correlation between l_i/q_{95} and ρ_{q2} is evident from the good clustering of the data along the line specified by equation 4. The horizontal blue line at $l_i/q_{95} = 0.28$ shows approximately where IRLM disruptivity transitions from low to high.

8.2. Decoupling effects of ρ_{q2} and l_i/q_{95} on IRLM disruptivity

In the previous section, it is assumed that l_i/q_{95} and ρ_{q2} are effectively equivalent, as suggested by equation 4. However, here we show that l_i/q_{95} has a stronger effect on IRLM disruptivity. Figure 19 shows all disruptive and non-disruptive IRLMs plotted in the 2D space of l_i/q_{95} and ρ_{q2} at 100 ms prior to mode termination.

The data in the region where $\rho_{q2} = [0.7, 0.8]$ show a clear vertical separation, rather than a horizontal one. For instance, choosing a threshold of $l_i/q_{95} < 0.28$ as the definition of a non-disruptive IRLM results in 7% mis-categorized disruptive IRLMs, and 24% mis-categorized non-disruptive IRLMs. To capture a similar number of correctly identified non-disruptive IRLMs using ρ_{q2} , a value of $\rho_{q2} < 0.78$ is used and results in 14% mis-categorized disruptive IRLMs, and 25% mis-categorized non-disruptive IRLMs. This confirms the result of figure 18 that l_i/q_{95} categorizes disruptive and non-disruptive IRLMs better than ρ_{q2} .

To reduce mis-categorized disruptive modes, a threshold of $l_i/q_{95} < 0.25$ can be used which produces only 3% mis-categorized disruptive IRLMs. However, the mis-categorized non-disruptive IRLMs increase to 42%.

8.3. d_{edge} discriminates disruptive IRLMs within 20 ms of disruption

In this subsection and subsection 8.4, it is assumed that the exponential $n = 1$ growth in B_R (figure 10c) is due to growth of the 2/1 island. It will be shown

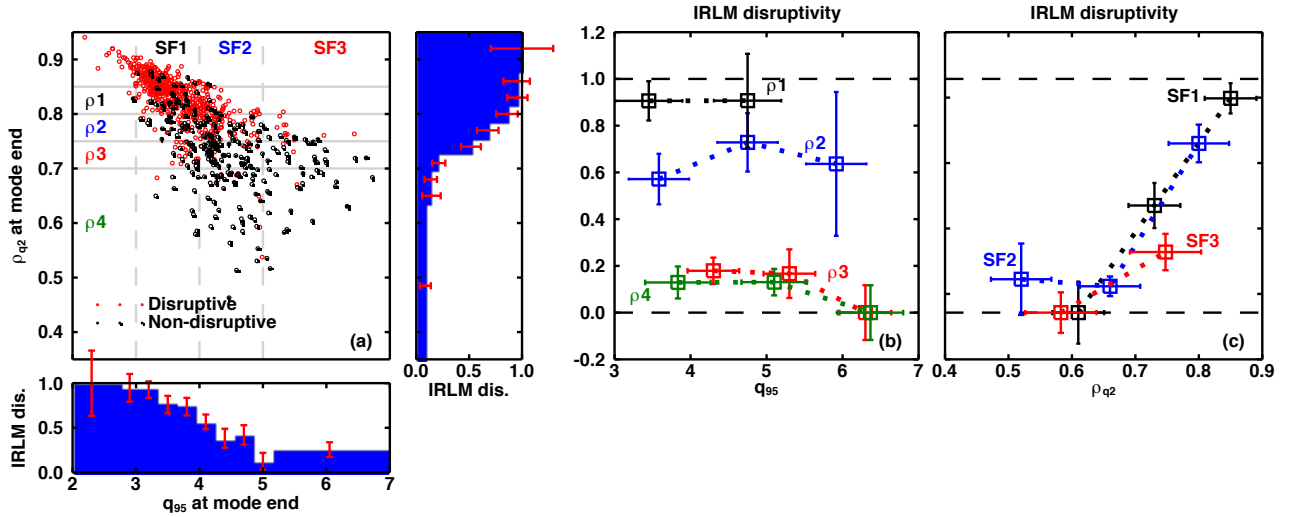


Figure 17. (a) The relationship of disruptive and non-disruptive IRLMs in q_{95} vs. ρ_{q2} space. One-dimensional IRLM disruptivity histograms in q_{95} and ρ_{q2} are shown on the bottom and right. Bins in ρ_{q2} and safety factor are shown in gray, for use in (b) and (c). Note that only the binning intervals are shown, and not the explicit bins (i.e. the dashed and solid gray lines are unrelated). (b) IRLM disruptivity in windows of ρ_{q2} as a function of q_{95} . (c) IRLM disruptivity in windows of q_{95} as a function of ρ_{q2} .

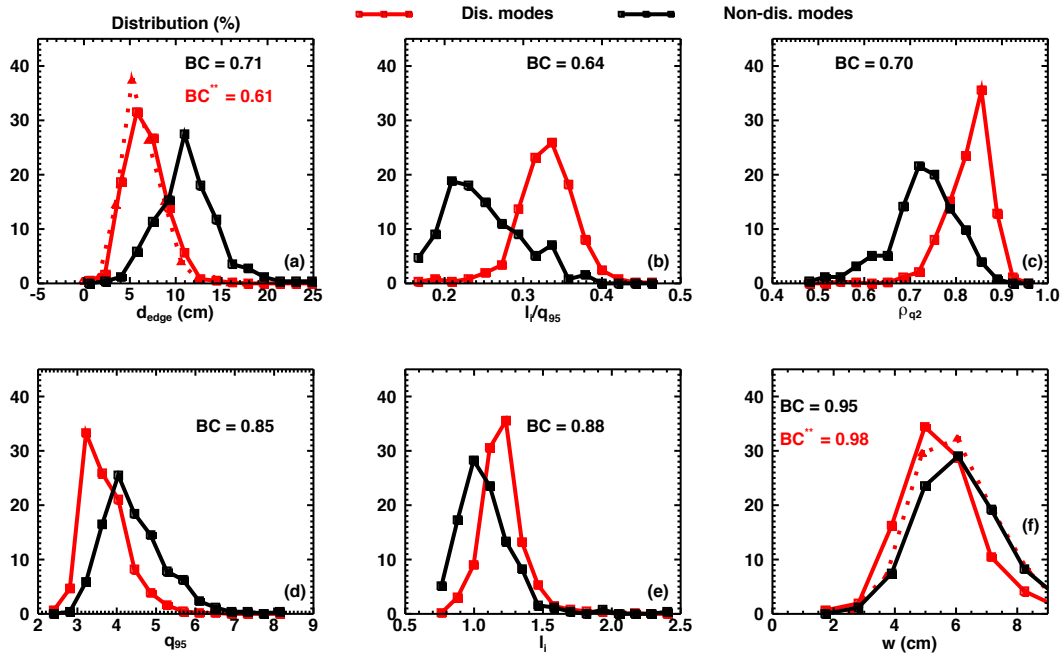


Figure 18. Disruptive and non-disruptive IRLM distributions are shown as a function of 6 parameters to reveal the dominant disruption predictor. Amount of overlap between distributions is quantified by the Bhattacharyya Coefficient (BC). A BC value of 0 indicates no overlap, and a value of 1 indicates complete overlap. Solid curves are evaluated at 100 ms before mode termination, while the dotted red in (a) and (f) are evaluated 20 ms before the disruption. Not shown, dq/dr_{q2} produces a value of $BC=0.89$.

here that d_{edge} is as effective as l_i/q_{95} at discriminating disruptive IRLMs within 20 ms of the disruption. A possible physical interpretation will be given in section 9.

Figure 20 shows the island half-width as a function of the distance between the $q = 2$ surface and the unperturbed plasma separatrix, $a - r_{q2}$. The shortest

perpendicular distance from the black dashed line representing the unperturbed last closed flux surface (LCFS) to a given point is what we have called $d_{edge} = a - (r_{q2} + w/2)$. In other words, a point appearing near the solid black line represents an island whose radial extent reaches near the unperturbed LCFS. Due to the perturbing field of the locked mode, we expect kinking

of the LCFS. This kinking of the LCFS is not accounted for in our calculation of d_{edge} .

d_{edge} is shown to separate disruptive and non-disruptive modes as effectively as ρ_{q2} at 100 ms prior to disruption in figure 18 (their BC values are considered equal to within error). Within 20 ms of the disruption, d_{edge} separates the two populations better with a BC value of 0.61 (compare the dotted red and solid black distributions for d_{edge} in figure 18). The better separation is due to the exponential growth of the $n = 1$ field that occurs in the final 50 ms before disruption: that growth of B_R and thus of w decreases d_{edge} without affecting ρ_{q2} . Note that evaluating d_{edge} at 20 ms prior to the disruption implicitly attributes the $n = 1$ exponential growth to a growing 2/1 island, but the validity of this assumption does not affect the discrimination ability of d_{edge} .

Choosing a threshold of $d_{edge} > 9$ cm evaluated 20 ms before the disruption (blue dashed line in figure 20), we find 8% mis-categorized disruptive IRLMs, and 28% mis-categorized non-disruptive IRLMs. This is comparable with the 7% and 24% found for $l_i/q_{95} < 0.28$, though l_i/q_{95} is evaluated 80 ms earlier (these thresholds on d_{edge} and l_i/q_{95} correctly categorize 195 and 194 non-disruptive IRLMs respectively). A more conservative threshold of $d_{edge} > 11$ cm produces 3% mis-categorized disruptive IRLMs, and 58% mis-categorized non-disruptive IRLMs.

8.4. Weak dependence of IRLM disruptivity on island width

The island width alone is found to be a poor discriminator of disruptive IRLMs at times 20 ms or prior to the disruption (figure 18f). From the time of saturation until ~ 20 ms prior to the disruption, disruptive and non-disruptive island widths are similar, with a slight tendency for non-disruptive modes to be larger at the earlier times. IRLM disruptivity as a function of the island half-width is shown in the histogram on the right of figure 20. For the majority of islands with half-widths between 2 and 5 cm, IRLM disruptivity does not change significantly, and might be constant within statistical error.

The region below the curved dashed line in figure 20 shows the approximate mode detection limit due to typical signal-to-noise-ratio discussed in section 2.4. Modes appearing in this region were once above the detection limit, and are still measured due to the asymmetry in onset and disappearance thresholds used in the analysis. It is possible that undetected modes in this region might affect the resulting IRLM disruptivity.

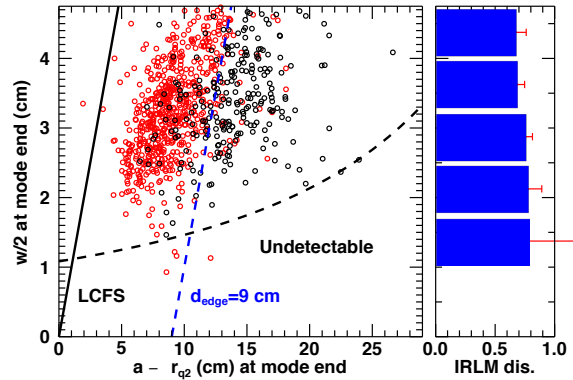


Figure 20. The assumption that the 2/1 island dominates the disruptive exponential growth is implicit in this figure, and therefore this figure is exploratory. The disruptive data are from 20 ms before disruption, and the non-disruptive data are from 100 ms before mode termination. The x -axis quantifies the distance of the $q = 2$ surface from the unperturbed last closed flux surface (LCFS). The shortest perpendicular distance from the unperturbed LCFS (black solid) to a given point is d_{edge} (i.e. $d_{edge} = a - (r_{q2} + w/2)$). The blue dashed line is where $d_{edge} = 9$ cm. IRLM disruptivity as a function of island half-width is shown in the blue histogram.

8.5. IRLM disruption prediction

Thus far we have discussed percent mis-categorizations, and similarly, separation of disruptive and non-disruptive distributions measured by the BC coefficient, at specific points in time. Although useful for understanding the physics of IRLM disruptions, single time-slice analysis is not sufficient for disruption prediction. Prediction during the locked phase requires establishing a parameter threshold that will never be exceeded by a non-disruptive IRLM, but will be exceeded by a disruptive IRLM *at some point* before the thermal quench.

We consider l_i/q_{95} and d_{edge} separately as IRLM disruption predictors. These predictors are intended to be used only in the presence of a detected locked mode. Table 2 shows the percent missed disruptions and percent false alarms for the given thresholds, and for the given warning times. The percent missed disruptions is defined as the number of disruptive IRLMs that do not exceed the threshold within X ms of the disruption, divided by the total number of disruptive IRLMs. The percent false alarms is defined as the number of non-disruptive IRLMs that exceed the threshold at any time during their lifetime, divided by all issued alarms.

Despite the seemingly short timescale, 20 ms is a sufficient amount of time to deploy massive gas injection in DIII-D [54].

Condition with IRLM	Mis. dis. (%) at 100 [20] ms	False alarms (%)
$l_i/q_{95} > 0.28$	6 [6]	13
$d_{edge} < 9$ cm	6 [4]	14
None	0 [0]	29

Table 2. IRLM disruption prediction statistics for l_i/q_{95} , d_{edge} , and no prediction parameter. The two thresholds are shown graphically by the dashed blue lines in figures 19 and 20 (note that figures 19 and 20 are evaluated at single time slices, whereas these statistics are evaluated over appropriate time intervals). These prediction criteria are intended for use in the presence of a detected IRLM only. The "None" condition shows the disruption statistics for the case where all IRLMs are considered disruptive.

8.6. Ramp-down IRLM disruptivity and ρ_{q2} evolution

In this section only, we extend our definition of disruption to include those that occur during I_p ramp-down.

Figure 21a shows the change in ρ_{q2} over the lifetime of IRLMs that either disrupt or decay/spin-up during the I_p flat-top. Figure 21b shows the same change in ρ_{q2} , but for IRLMs which are terminated by the I_p ramp-down (i.e. IRLMs that disrupt or decay during ramp-down). An increase in IRLM disruptivity for modes with $\rho_{q2} > 0.75$ at mode end is less pronounced for ramp-down modes in figure 21b than flat-top modes in figure 21a. A study of the trajectories in l_i and q_{95} space, similar to that done in reference [3] for ramp-up, might provide insight into why IRLM disruptivity is decreased for ramp-down.

In contrast to the decreased IRLM disruptivity observed during ramp-downs here, born locked modes on JET [55] were observed to disrupt during current ramp-down. These JET discharges were run at $q_{95} = 3.5$ (corresponding to $\rho_{q2} > 0.8$ on a typical DIII-D discharge). The IRLM disruptivity for $\rho_{q2} > 0.8$ in figure 21b is $\sim 40\%$, in contrast to the JET experiments where the majority were observed to disrupt. However, the DIII-D discharges were error-field-corrected, while the JET ones were not, which might explain the higher disruptivity. In addition, it is possible that born locked modes and IRLMs respond differently to plasma ramp-downs.

The evolution of ρ_{q2} between locking and mode end, provides insight into the evolution of both l_i/q_{95} and d_{edge} . Figure 21a shows that ρ_{q2} tends to increase by $\sim 5\%$ between locking and mode end. This is noticeable by the clustering of points above the dashed diagonal. Equation 4 suggests that an increase in ρ_{q2} at fixed q_{95} implies an increase in l_i . As I_p , B_T , and plasma shaping are fixed via feedback in most DIII-D discharges, the assumption of constant q_{95} is very reasonable. The increase in l_i during locked modes agrees with earlier works [12, 13, 14]. About 25 non-disruptive IRLMs move inward (figure 21b), likely as a

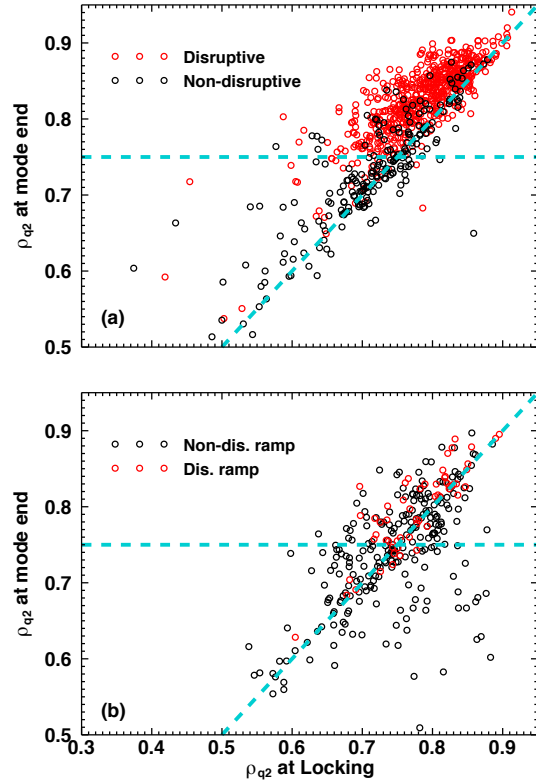


Figure 21. (a) The evolution of ρ_{q2} from locking to mode end (100 ms prior to mode termination) for IRLMs which terminate during the I_p flat-top. The diagonal line represents unchanging ρ_{q2} . The horizontal line is at $\rho_{q2} = 0.75$, and marks the approximate transition from low to high IRLM disruptivity. (b) Same as (a) for modes which are terminated by an I_p ramp-down. A smaller fraction of disruptive modes exists here.

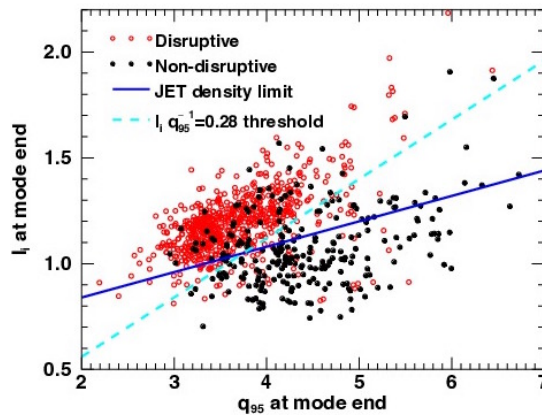


Figure 22. All disruptive and non-disruptive IRLMs shown in l_i vs. q_{95} space. The JET density limit shown in blue defines the lower bound of the disruptive locked modes in DIII-D remarkably well. The cyan dashed line is the $l_i/q_{95} = 0.28$ value again, first seen in figure 19 to divide the populations well.

result of the increasing q_{95} as I_p is reduced, which on a resistive timescale also changes the position of the $q = 2$ surface.

9. Discussion

The physical significance of l_i/q_{95} might be related to the potential energy for tearing growth (i.e. to the classical stability index Δ') [56, 41]. Therefore, l_i/q_{95} might distinguish whether an IRLM will undergo exponential growth when locked, and since this growth is common to disruptive IRLMs, it would explain why l_i/q_{95} performs well as a disruption predictor. Separately, it is interesting that a high value of l_i is itself unstable, causing radiative contraction of the temperature and current profiles [13], which further increases l_i . Since q_{95} is approximately fixed via feedback, increasing l_i implies increasing l_i/q_{95} .

Alternatively, the physical significance of l_i/q_{95} might be related to an excess of radiative losses in the island, overcoming the Ohmic heating, resulting in exponential growth [57]. Figure 22 shows good separation of disruptive and non-disruptive IRLMs in the l_i vs. q_{95} space used in reference [13] to identify density limit disruptions. Although the plasmas discussed herein are expected to be far from the density limit [58] as a result of the degraded confinement, they are likely near the radiation instability limit which is theorized as the fundamental mechanism causing the density limit [59]. This radiation instability limit is expected qualitatively to scale with l_i/q_{95} .

Although the underlying physics of d_{edge} is not investigated here, other works have found similar parameters to be relevant to the onset of the thermal quench, and are briefly listed here. In reference [40], a stable Alcator C-Mod equilibrium is used as an initial condition for a numerical simulation of massive gas injection. It is found that by uniformly distributing a high-Z gas in the edge, a 2/1 island is driven unstable and upon intersecting with the high-Z gas (i.e. when d_{edge} becomes small), the 2/1 grows rapidly followed by a 1/1 tearing mode that leads to a complete thermal quench. Similarly, a limited plasma is simulated in reference [41] with a current profile unstable to the 2/1 island, and the plasma current is ramped up to drive the 2/1 island towards the plasma edge. It is found that when the 2/1 island comes into contact with the limiter or a cold edge region (i.e. in both cases, when d_{edge} is small), a rapid growth of the 2/1 ensues followed by a 1/1 kink displacement of the core, ending in a disruption. Similarly, experimental results of disruptions induced by EF penetration modes on COMPASS-C [39] are attributed to exceeding a threshold of $w/(a - r_s) > 0.7$, where w and r_s are the 2/1 island width and minor radius, which is thought to be due to the 2/1 island interacting with 3/1 island.

Large 3-D fields at the plasma separatrix cause radial deformations of the edge plasma, leading to edge flux-surfaces (like the $q = 2$ when d_{edge} is small) intersecting the vessel [60]. Further, some works

suggest the existence of a stochastic layer within the LCFS [61, 62], which might facilitate stochastization of the 2/1 island when d_{edge} is sufficiently small.

Separately, the radiation drive of tearing modes is sensitive to edge proximity [57], causing island growth which reduces d_{edge} , and could then lead to the thermal quench through one of the above mechanisms. Again, recall that our interpretation of d_{edge} at 20 ms prior to the disruption requires the exponential growth observed in the $n = 1$ B_R signal to be due to the 2/1 island growth, which is plausible but not confirmed due to lack of poloidal harmonic analysis in the locked phase. Regardless of the theoretical interpretation, d_{edge} is a useful IRLM disruption predictor within 20 ms of the disruption for DIII-D.

Summary and conclusions

Approximately 22,500 DIII-D plasma discharges were automatically analyzed for the existence of initially rotating 2/1 locked modes (IRLMs). The results of this analysis permit statistical analysis of timescales, mode amplitude dynamics, effects of plasma β and major radius R , and disruptivity as a function of plasma and mode properties.

Timescales investigated suggest that a rotating 2/1 NTM that will eventually lock rotates for ~ 200 ms, decelerates from $f = 2$ kHz to locked in ~ 15 ms, and survives as a locked mode for ~ 300 ms (these values all represent the most frequent value in their respective histograms). These timescales provide insight into how quickly a disruption mitigation system must respond if operational alarms are set at various points during the lifetime of the IRLM.

Prior to disruption, the median $n = 1$ perturbed field grows exponentially with an e -folding time between $\tau_g = [80, 250]$ ms, which might be due to exponential growth of the 2/1 IRLM.

The parameter l_i/q_{95} is shown to have a strong ability to discriminate between disruptive and non-disruptive IRLMs, up to hundreds of milliseconds before the disruption. From a disruption prediction standpoint, l_i/q_{95} provides the most forewarning, and the lowest missed disruptions and false alarms. As an example, the criterion $l_i/q_{95} < 0.28$ misses 6% of disruptions and produces 13% false alarms, with at least 100 ms of warning time. l_i/q_{95} might be related to the free energy available for tearing mode growth.

Within 20 ms of the disruption, d_{edge} performs comparably to l_i/q_{95} in its ability to discriminate disruptive IRLMs. A threshold above which IRLMs are considered non-disruptive of $d_{edge} = 9$ cm produces 4% missed disruptions and 14% false alarms, with at least 20 ms of warning time. d_{edge} is also observed to exhibit the best correlation with the IRLM survival

time.

Although from a disruption prediction standpoint d_{edge} is less useful than l_i/q_{95} due to the shorter warning time, it might be a fundamental trigger of the thermal quench, supported by similar observations by other authors [39, 41, 40, 60].

Future work will attempt to validate thermal quench onset mechanisms in plasmas with locked modes, with the goal of a fundamental understanding of locked mode disruptions, and thus how to avoid them.

10. Acknowledgements

This work was conducted in part under the DOE Grant DE-SC0008520. In addition, this work is supported by the U.S. Department of Energy, Office of Science, Office of Fusion Energy Sciences, using the DIII-D National Fusion Facility, a DOE Office of Science user facility under awards, DE-FG02-04ER54761¹, DE-FC02-04ER54698², and DE-FG02-92ER54139³. DIII-D data shown in this paper can be obtained in digital format by following the links at https://fusion.gat.com/global.D3D_DMP.

The authors would like to thank E.J. Strait and R.J. Buttery for carefully reading the manuscript, and J. Hanson, E. Kolemen, M. Lanctot, L. Lao, C. Paz-Soldan, D. Shiraki, and R. Wilcox for fruitful conversations that contributed to this work. The authors would also like to thank S. Flanagan and D. Miller for their computer expertise in developing this database, and M. Brookman for assistance in preparing the electron cyclotron emission data.

References

- [1] T.C. Hender, J.C. Wesley, et al. *Nucl. Fusion*, 47:S128–S202, 2007.
- [2] R.J. La Haye et al. *Phys. Plasmas*, 10(9), 2003.
- [3] J.A. Snipes et al. *Nucl. Fusion*, 28(6), 1988.
- [4] R. Fitzpatrick. *Nucl. Fusion*, 33(7), 1993.
- [5] J.L. Luxon. *Nucl. Fusion*, 42:614–633, 2002.
- [6] R.J. Buttery et al. *Plasma Phys. Contr. Fusion*, 42:B61–B73, 2000.
- [7] P.H. Rutherford. *Phys. Fluids*, 16(11), 1973.
- [8] R.B. White, D.A. Monticello, and M.N. Rosenbluth. *Phys. Rev. Lett.*, 39(25), 1977.
- [9] Z. Chang, J.D. Callen, E.D. Fredrickson, et al. *Phys. Rev. Lett.*, 74(23), 1995.
- [10] R.J. La Haye. *Phys. Plasmas*, 13(055501), 2006.
- [11] Z. Chang and J.D. Callen. *Nucl. Fusion*, 30(2), 1990.
- [12] J.T. Scoville, R.J. La Haye, et al. *Nucl. Fusion*, 31(5), 1991.
- [13] J.A. Wesson, R.D. Gill, M. Hugon, F.C. Schüller, J.A. Snipes, D.J. Ward, et al. *Nucl. Fusion*, 29(4), 1989.
- [14] F.C. Schüller. *Plasma Phys. Contr. Fusion*, 37:A135–A162, 1995.
- [15] P.C. de Vries, M.F. Johnson, I. Segui, et al. *Nucl. Fusion*, 49(055011), 2009.
- [16] P.C. de Vries and M.F. Johnson. *Nucl. Fusion*, 51(053018), 2011.
- [17] S.P. Gerhardt et al. *Nucl. Fusion*, 53(043020), 2013.
- [18] S.P. Gerhardt, D.S. Darrow, et al. *Nucl. Fusion*, 53(063021), 2013.
- [19] A.M. Garofalo et al. *Fusion Eng. Des.*, 89:876–881, 2014.
- [20] B. Cannas, A. Fanni, G. Pautasso, G. Sias, et al. *Fusion Eng. Des.*, 86:1039–1044, 2011.
- [21] G. Pautasso, C. Tichmann, S. Egorov, T. Zehetbauer, et al. *Nucl. Fusion*, 42:100–108, 2002.
- [22] G.A. Rattá, J. Vega, A. Murari, G. Vagliasindi, M.F. Johnson, P.C. de Vries, et al. *Nucl. Fusion*, 50(025005), 2010.
- [23] R. Yoshino. *Nucl. Fusion*, 43:1771–1786, 2003.
- [24] C.G. Windsor, G. Pautasso, C. Tichmann, R.J. Buttery, T.C. Hender, et al. *Nucl. Fusion*, 45:337–350, 2005.
- [25] J.V. Hernandez, A. Vannucci, T. Tajima, Z. Lin, W. Horton, and S.C. McCool. *Nucl. Fusion*, 36(8), 1996.
- [26] A. Sengupta and P. Ranjan. *Nucl. Fusion*, 40(12), 1993.
- [27] D. Wróblewski and G.L. Jahns. *Nucl. Fusion*, 37(6), 1997.
- [28] Y. Zhang, G. Pautasso, et al. *Nucl. Fusion*, 51(063039), 2011.
- [29] R.J. Buttery et al. *Nucl. Fusion*, 44:1027–1035, 2004.
- [30] P.C. de Vries, G. Pautasso, E. Nardon, et al. *Nucl. Fusion*, 56(026007), 2016.
- [31] K.E.J. Olofsson, J.M. Hanson, D. Shiraki, F.A. Volpe, et al. *Plasma Phys. Contr. Fusion*, 56(095012), 2014.
- [32] E.J. Strait. *Rev. Sci. Instrum.*, 77(023502), 2006.
- [33] J.D. King, E.J. Strait, R.L. Boivin, D. Taussig, M.G. Watkins, et al. *Rev. Sci. Instrum.*, 85(083503), 2014.
- [34] V. Riccardo et al. *Plasma Phys. Contr. Fusion*, 52(124018), 2010.
- [35] M.E. Austin and J. Lohr. *Rev. Sci. Instrum.*, 74(3), 2003.
- [36] D. Shiraki, R.J. La Haye, N.C. Logan, E.J. Strait, and F.A. Volpe. *Nucl. Fusion*, 54(033006), 2014.
- [37] L.L. Lao, H. St. John, and R.D. Stambaugh. *Nucl. Fusion*, 25(10):1421–1436, 1985.
- [38] B.W. Rice, D.G. Nilson, and D. Wróblewski. *Rev. Sci. Instrum.*, 66(1):373–375, 1995.
- [39] T.C. Hender, R. Fitzpatrick, A.W. Morris, et al. *Nucl. Fusion*, 32(12), 1992.
- [40] V.A. Izzo. *Nucl. Fusion*, 46:541–547, 2006.
- [41] A. Sykes and J.A. Wesson. *Phys. Rev. Lett.*, 44(18), 1980.
- [42] R.J. La Haye and J.T. Scoville. *Rev. Sci. Instrum.*, 62:2146–2153, 1991.
- [43] J.L. Luxon, M.J. Schaffer, et al. *Nucl. Fusion*, 43:1813–1828, 2003.
- [44] H. Zohm, M. Maraschek, G. Pautasso, M. Schittenhelm, S. Sesnic, M. Sokoll, and W. Suttrop. *Plasma Phys. Contr. Fusion*, 37:A313–A324, 1995.
- [45] V. Igochine, O. Dumbrajs, D. Constantinescu, H. Zohm, G. Zvejnicks, et al. *Nucl. Fusion*, 46:741–751, 2006.
- [46] P.C. de Vries, G. Waidmann, A.J.H. Donné, and F.C. Schüller. *Plasma Phys. Contr. Fusion*, 38:467–476, 1996.
- [47] R.J. Buttery, R.J. La Haye, et al. *Phys. Plasmas*, 15(056115), 2008.
- [48] R.J. La Haye and O. Sauter. *Nucl. Fusion*, 38(7), 1998.
- [49] L. Urso, H. Zohm, et al. *Nucl. Fusion*, 50(025010), 2010.
- [50] Kyungjin Kim, Yong-Su Na, Minhwa Kim, et al. *Curr. Appl. Phys.*, 15:547–554, 2015.
- [51] R. Fitzpatrick. *Phys. Plasmas*, 5(9), 1998.
- [52] A. Bhattacharyya. *Indian J. Statistics*, 7(4), 1946.
- [53] D. Comaniciu and V. Ramesh. *Comput. Vision Pattern Recog.*, 2:142–149, 2000.
- [54] N.W. Eidietis et al. *Nucl. Fusion*, 55(063030), 2015.
- [55] R.J. Buttery, M. De’ Benedetti, T.C. Hender, and B.J.D. Tubbing. *Nucl. Fusion*, 40(4), 2000.
- [56] C.Z. Cheng, H.P. Furth, and A.H. Boozer. *Plasma Phys. Contr. Fusion*, 29(3):351–366, 1987.
- [57] R.B. White, D.A. Gates, and D.P. Brennan. *Phys. Plasmas*, 22(022514), 2015.
- [58] M. Greenwald, J.L. Terry, and S.M. Wolfe. *Nucl. Fusion*,

- 28(12), 1988.
- [59] D.A. Gates and L. Delgado-Aparicio. *Phys. Rev. Lett.*, 108(165004), 2012.
- [60] T.E. Evans, R.K.W. Roeder, J.A. Carter, B.I. Rapoport, M.E. Fenstermacher, and C.J. Lasnier. *J. Phys.*, Conference Series 7:174–190, 2005.
- [61] T.E. Evans, R.A. Moyer, and P. Monat. *Phys. Plasmas*, 9(12), 2002.
- [62] V.A. Izzo and I. Joseph. *Nucl. Fusion*, 48(115004), 2008.
- [63] J.A. Wesson, D.J. Campbell, J.W. Connor, R.D. Gill, J. Hugill, C.N. Lashmore-Davies, G.M. McCracken, H.R. Wilson, et al. *Tokamaks*, page 366. Clarendon Press - Oxford, third edition, 2004.

Appendix A

A model was produced to map from the value of the $n = 1$ major-radial magnetic field B_R at the external saddle loops to the perturbed current carried by a circular cross-section toroidal current sheet. The current sheet has major radius R and minor radius r_{q2} , derived from equilibrium reconstructions using magnetics and Motional Stark Effect data. A shaping study was performed to test the impact of ellipticity on the $n = 1$ external saddle loop measurement. The impact was found to be relatively small, introducing corrections of less than 5%. Hence, it was concluded that circular cross-sections are sufficient for modeling external saddle loop signals for the sake of the present study.

The modeled current sheet is discretized into N helical wire filaments with $2/1$ pitch giving a toroidal spacing of $360/N$ degrees. The currents are distributed among the wires to produce a $2/1$ current perturbation as shown by the colors in figure 23 (black represents no perturbed current and red represents maximum perturbed current).

The field is calculated by numerically integrating the Biot-Savart Law along each wire. Figure 23b shows the resulting major-radial field B_R as "seen" by the external saddle loops, due to a $2/1$ current distribution. The color contour shows a clear $n = 1$ field distribution. Although the external saddle loops have complete toroidal coverage, they have only $\sim 25\%$ poloidal coverage for the non-elongated, cylindrically approximated plasma.

A single measurement at each saddle loop is estimated by averaging the field at 100 sample points. Care was taken to ensure the area of each sample point is identical, which simplifies the flux calculation. The field samples are averaged, which is identical to calculating the total flux and dividing by saddle loop area A_{sl} :

$$\frac{\sum_{i=1}^n B_{R,i} a_i}{A_{sl}} = \frac{a}{na} \sum_{i=1}^n B_{R,i} = \frac{1}{n} \sum_{i=1}^n B_{R,i} \quad (6)$$

where A_{sl} is the total area of one saddle loop, a_i is the constant sample area (i.e. $a_i = a$), n is the

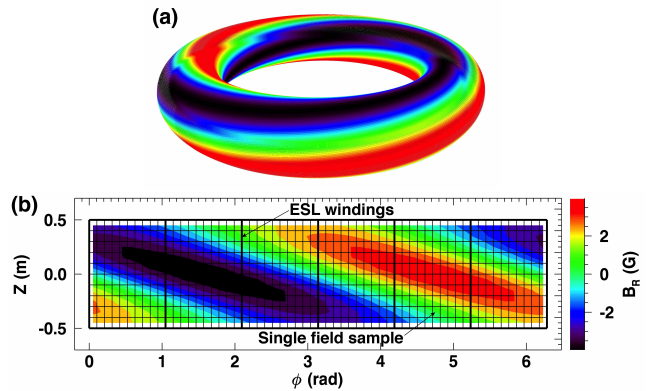


Figure 23. (a) A 3D filament model of a $2/1$ tearing mode used to map from the radial field at the external saddle loops B_R to a perturbed island current δI . (b) The radial field at the external saddle loops is shown in the color contour for a mode carrying 3.14 kA of $n = 1$ current. The thick black lines outline the six external saddle loops. The thin black lines define cells of equal area, which are used to sample the field to compute an average over the loop.

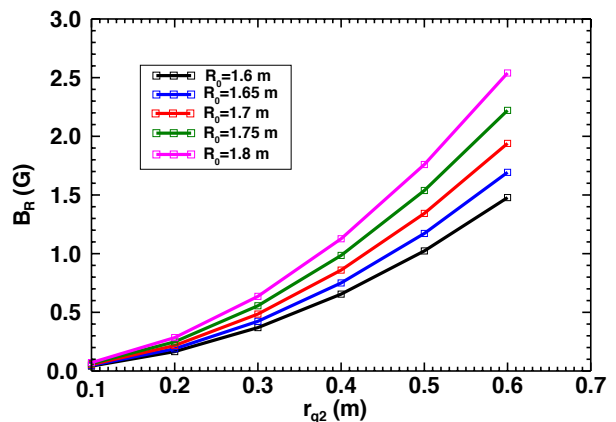


Figure 24. The $n = 1$ major-radial field B_R measured at the saddle loops as a function of the minor radius of the $q = 2$ surface r_{q2} .

number of sample regions per saddle loop, and $B_{R,i}$ is the major-radial field at the i^{th} sample region.

The above averaging is done for each of the six saddle loops. The simulated signals are then pair-differenced, and a least squares fit is used to extract the amplitude of the $n = 1$ component, in the same way as experimental data are analyzed in section 2.4.

The island current, δI , is defined as the total current deficit, as seen in figure 25b. A second definition of island current is useful for mapping to a cylindrical island width, being half the sinusoidal perturbed current δI_h (see figure 25a). δI_h and δI are related by the equation $\delta I = \pi \delta I_h$. The current distribution in figure 25b can be seen as the superposition of the distribution in 25a, plus an

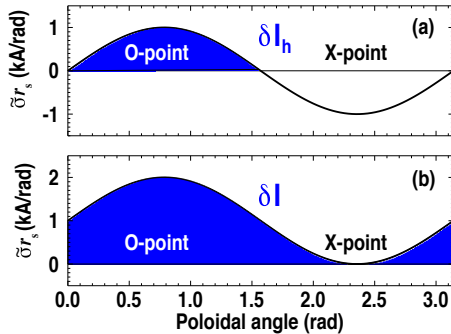


Figure 25. (a) Half the perturbed island current δI_h is shown by the blue shaded region. Here, it is assumed that the current perturbation is sinusoidal about zero. (b) The total perturbed island current δI is shown by the blue shaded region. Here, it is assumed that no perturbed current flows at the X-point.

axisymmetric current. The non-axisymmetric fields produced by 25a and 25b are identical.

The $n = 1$ B_R component in the external saddle loops, B_R^1 , was then studied as a function of R and r_{q2} for fixed island current δI_h as seen in figure 24. B_R^1 is found to be quadratic in r_{q2} in agreement with the cylindrical approximation. As R is increased, the leading order coefficient of the quadratic is seen to increase as well. Defining the leading order coefficient $\alpha[R]$ (which note is a function of R), we find the following relationship:

$$B_R^1 = \alpha[R] \delta I_h (r_{q2})^2 \quad (7)$$

where B_R^1 is in Gauss, δI_h is in kA, r_{q2} and R are in meters, and α has units of G/kA/m². Evaluating the change in α as a function of R , the dependence is found to be well approximated by a second order polynomial $\alpha[R] = aR^2 + bR + c$ where $a = 19.15$ G/kA/m⁴, $b = -50.40$ G/kA/m³, and $c = 35.71$ G/kA/m².

With equation 7, experimental $n = 1$ measurements from the external saddle loops are mapped to δI_h by a simple inversion of the equation and with major and minor radii provided by EFIT informed by magnetics and Motional Stark Effect data:

$$\delta I_h = \frac{B_R^1}{\alpha[R](r_{q2})^2} \quad (8)$$

Appendix B

Although the perturbed island current δI is an intrinsic island quantity that accounts for toroidicity, an island width was desirable for some studies. We will use δI to map to an island width.

We solve for the radial field at the $q = 2$ surface \tilde{B}_r by assuming cylindrical geometry and using the ordering $k_\theta = m/r \gg k_z = n/R$. The

non-axisymmetric field $\tilde{\mathbf{B}}$ produced by the island is expressed as

$$\tilde{\mathbf{B}} = \nabla \times \Psi \hat{\mathbf{z}} \quad (9)$$

where Ψ is the perturbed flux function which is of the form $\Psi = \psi(r)e^{im\theta}$. We assume the perturbed current in the island $\tilde{\mathbf{j}}$ to be a sheet current located at the $q = 2$ surface expressed as

$$\tilde{\mathbf{j}} = \tilde{\sigma} \sin(2\theta) \delta(r_{q2} - r) \hat{\mathbf{z}} \quad (10)$$

where $\tilde{\sigma}$ is constant with units (A/m), $\delta(\dots)$ represents the Dirac delta function, and the poloidal harmonic $m = 2$ is implied. Invoking Ampere's law where the time derivative of \mathbf{E} is neglected (the characteristic velocity of the system $v \ll c$), we find

$$-\nabla^2 \Psi = \mu_0 \tilde{\sigma} \sin(2\theta) \delta(r_{q2} - r) \quad (11)$$

Solving the cylindrical Laplacian both inside and outside the $q = 2$ surface, requiring the solutions be continuous across r_{q2} , and defining the jump in the radial derivative with the radial integral of $\tilde{\mathbf{j}}$, we find

$$\Psi = \frac{\mu_0 \tilde{\sigma}}{4} \sin(2\theta) \begin{cases} \frac{r^2}{r_{q2}} & \text{for } r < r_{q2} \\ \frac{r_{q2}^3}{r^2} & \text{for } r \geq r_{q2} \end{cases} \quad (12)$$

The field at the $q = 2$ surface is then given by

$$\tilde{\mathbf{B}}_{q2} = \frac{\mu_0 \tilde{\sigma}}{2} [\cos(2\theta) \hat{r} + \sin(2\theta) \hat{\theta}] \quad (13)$$

We now want to replace $\tilde{\sigma}$ with an expression for δI . We do so as follows (see figure 25a)

$$\delta I_h \equiv \int_0^{\pi/2} \int_{r_{q2-}}^{r_{q2+}} \tilde{\mathbf{j}} \cdot d\mathbf{A} \quad (14)$$

where $d\mathbf{A} = r dr d\theta \hat{\mathbf{z}}$, and $r_{q2\pm} = r_{q2} \pm w/2$. After substituting equation 10 and evaluating the integral, we find $\tilde{\sigma} = \delta I_h / r_{q2}$.

Finally, substituting this into equation 13, we have,

$$\tilde{\mathbf{B}}_{q2}(\delta I) = \frac{\mu_0 \delta I_h}{2r_{q2}} [\cos(2\theta) \hat{r} + \sin(2\theta) \hat{\theta}] \quad (15)$$

The cylindrical island width is given by [63]

$$w = c \left[\frac{16R\tilde{B}_r q^2}{mB_T dq/dr} \right]^{1/2} \quad (16)$$

where c is a toroidal correction for island widths measured at the outboard midplane, \tilde{B}_r is the perturbed radial field at the $q = 2$ surface, $q = 2$ is the local safety factor, $m = 2$ is the poloidal harmonic, B_T is the toroidal field at the magnetic axis, and dq/dr is the radial derivative of the safety factor evaluated at r_{q2} on the outboard midplane (the cylindrical expression for the safety factor $q = rB_T/(RB_\theta)$ was

used here). Substituting $q = 2$ and $m = 2$ and using the maximum of equation 15 for \tilde{B}_r , we have

$$w = c \left[\frac{16R}{B_T dq/dr} \frac{\mu_0 \delta I_h}{r_{q2}} \right]^{1/2} \quad (17)$$

This expression for the island width was validated against island widths identified using the electron cyclotron emission diagnostic [35]. For nine islands, equation 17 (with $c = 2/3$) estimated the island widths to be systematically $\sim 25\%$ too large, with a standard deviation of $\sim 25\%$. We therefore reduce c by 20%, to $c = 8/15$, and expect a 25% statistical error on island width estimates. This expression of the island width is used for all plots of w and $d_{overlap}$.